



# Research Repository UCD

<b>Title</b>	The Use of the Forced Frequency of a Bridge Due to a Truck Fleet for Estimating Stiffness Losses at Low Speed
<b>Authors(s)</b>	González, Arturo, Feng, Kun, Casero, Miguel
<b>Publication date</b>	2022-11-09
<b>Publication information</b>	González, Arturo, Kun Feng, and Miguel Casero. "The Use of the Forced Frequency of a Bridge Due to a Truck Fleet for Estimating Stiffness Losses at Low Speed." MDPI, November 9, 2022. <a href="https://doi.org/10.3390/app122211380">https://doi.org/10.3390/app122211380</a> .
<b>Publisher</b>	MDPI
<b>Item record/more information</b>	<a href="http://hdl.handle.net/10197/13253">http://hdl.handle.net/10197/13253</a>
<b>Publisher's version (DOI)</b>	<a href="https://doi.org/10.3390/app122211380">10.3390/app122211380</a>

Downloaded 2025-12-04 23:03:37

The UCD community has made this article openly available. Please share how this access benefits you. Your story matters! (@ucd\_oa)



© Some rights reserved. For more information

## Article

# The Use of the Forced Frequency of a Bridge Due to a Truck Fleet for Estimating Stiffness Losses at Low Speed

Arturo González \*, Kun Feng and Miguel Casero

School of Civil Engineering, University College Dublin, D04 V1W8 Dublin, Ireland;  
kun.feng@ucdconnect.ie (K.F.); miguel.casero@ucd.ie (M.C.)

\* Correspondence: arturo.gonzalez@ucd.ie

**Abstract:** The influence of traffic loads on the dynamic features of a bridge is an external factor that can hinder the true condition of the structure. This paper aims to effectuate a shift in the way this factor is viewed. If the interaction between vehicle and bridge is modeled using the finite element method, the response is based on mass, stiffness, and damping matrices of a coupled vehicle-bridge system that vary with the location of the load at each point in time. The time-varying forced frequencies of a beam bridge model due to a fleet of 3-axle trucks based on eigenvalue analysis (i.e., derived from the matrices of the coupled system) are compared to those obtained using dynamic transient analysis (i.e., derived from the frequency content of the acceleration response of the beam due to a truck crossing). Truck properties are randomly varied within a realistic range to obtain a pattern for the forced vibration due to a truck fleet traveling at an ideal speed of 1 m/s on a 15 m bridge with a smooth surface, and at 10 m/s on a 30 m bridge. These patterns reveal a trend that allows for locating and quantifying the stiffness loss associated with a crack using only the forced frequency. The implementation of this methodology requires the installation of accelerometers on the bridge, and a nearby weigh-in-motion system to identify the traffic fleet of interest. High requirements for frequency resolution limit the application to bridges located on low speed routes.

**Keywords:** vehicle bridge interaction; damage detection; forced vibration; bridge dynamics; structural health monitoring; frequency evolution; mahalanobis distance; truck fleet

**Citation:** González, A.; Feng, K.; Casero, M. The Use of the Forced Frequency of a Bridge Due to a Truck Fleet for Estimating Stiffness Losses at Low Speed. *Appl. Sci.* **2022**, *12*, 11380. <https://doi.org/10.3390/app122211380>

Academic Editor(s): José António Correia and Junhong Park

Received: 1 September 2022

Accepted: 7 November 2022

Published: 9 November 2022

**Publisher's Note:** MDPI stays neutral with regard to jurisdictional claims in published maps and institutional affiliations.



**Copyright:** © 2022 by the authors. Licensee MDPI, Basel, Switzerland.

This article is an open access article distributed under the terms and conditions of the Creative Commons Attribution (CC BY) license (<https://creativecommons.org/licenses/by/4.0/>)

## 1. Introduction

The dynamic parameters associated with a bridge are employed by vibration-based structural health monitoring (SHM) methods for damage to be either detected (known as 'level I' damage detection methods), detected and located ('level II' methods), or detected, located, and quantified ('level III' methods). There is also a 'level IV' group of methods that not only detects, locates and quantifies damage, but also estimates the remaining life of the structure [1]. These dynamic parameters can be divided into two categories [2,3]:

- Those directly related to the main modes of vibration of the structure such as natural frequencies, damping, mode shapes, frequency contour, nodes position, modal assurance criteria, mode shape curvature, modal strain energy, etc.;
- Others such as coupling measurements, anti-resonances, frequency response functions, cumulative absolute velocity, cumulative absolute displacement, distributed vibration intensity, mean cumulative vibration intensity, etc.;

Accurate measurements of sophisticated dynamic parameters, i.e., mode shape curvature, come at a cost, and typically require sensors (i.e., accelerometers) installed at more locations and with a higher resolution than needed for extracting simpler parameters. For instance, a low number of accelerometers may be insufficient to capture a curvature change in the mode shape associated with the location of damage, but it can easily capture a shift in natural frequencies. The magnitude of this shift can be associated with a localized

bending stiffness loss and will depend on the severity and the relative position of the stiffness loss within the mode shape. In theory, frequencies can be obtained by simulating damage at different locations on a mathematical model of the structure, and then comparing with measured frequencies to locate the damage. In practice, damage is difficult to characterize from frequencies alone due to the need to capture multiple modes, the sensitivity to noise, operational and environmental loading, the dependence on the selected damage and structural models, and the non-uniqueness of the solution. Therefore, civil engineering structures are in urgent need of reliable assessment methods based only on the first few modes with simple assumptions about the behavior of the structure [4].

If traffic was used as the excitation force and the bridge was model-led using a finite element approach based on linear elastic elements, the frequencies of the bridge in free vibration are related to the time-invariant mass, stiffness, and damping matrices of the bridge. Nevertheless, periods of forced vibration involving vehicle-bridge interaction (VBI) will be difficult to avoid in locations where heavy traffic occurs regularly. The frequency content of the response due to traffic will differ in free and forced vibration according to the mass and frequency ratios of the vehicle to the bridge [5–7]. Shifts in forced frequency are affected by damage to an extent that varies with the location of the vehicle on the bridge [8].

Recently, the concept of using a traffic fleet to monitor bridges has drawn the interest of many researchers. For instance, Cantero and González [9] developed a level I damage detection technique that is based on the correlation between the weights measured by a pavement-based weigh-in-motion (WIM) system installed near the bridge, and the weights obtained by a bridge-based weigh-in-motion (BWIM) system for a specific truck fleet. WIM systems measure axle weights, spacings between axles, and the speed of the overpassing vehicles without interruption to the traffic flow. In the case of pavement-based systems, the sensors (i.e., piezoelectric, bending plate, load cell) are embedded in the road [10–12]. In the case of bridge-based systems, the sensors (i.e., strain gauges) are attached to the soffit of a bridge deck. Traditional BWIM algorithms relate the measured response, usually strains, to the axle weights through the influence line [13]. More complex BWIM algorithms apply moving force identification theory [14], but are difficult to implement in practice. OBrien et al. [15] explore the use of accelerations as input to a traditional BWIM algorithm to detect damage in a bridge from the weights inferred for a truck fleet. The algorithm is tested with one year of experimental data from a short-span reinforced concrete bridge in Slovenia. Further on, Wang et al. [16] apply the same concept based on the acceleration response to detect global damage, but using a moving force identification algorithm to estimate the weights of the vehicles. Following the same principle of detecting damage from deviations in BWIM results, OBrien et al. [17] use a traditional static algorithm that adopts the rotation response of the bridge as input. The rotation of 2D and 3D numerical bridge models due to real traffic fleets from a WIM site in Virginia (US) (i.e., almost 160,000 5-axle trucks recorded over a period of 4 years) is used for assessment purposes.

While the aforementioned publications deal with direct methods, i.e., measurements taken from sensors installed in the bridge, there is also an increasing interest in indirect methods such as vehicular measurements while crossing a bridge [18–20]. The latter is the line of research followed by Corbally and Malekjafarian, who derive the response of the contact point between the wheel and the bridge from sensors mounted on the vehicle for damage detection purposes [21]. The method is applied to a monitoring campaign using a vehicle fleet for a period of 2 years by means of theoretical simulations [22]. The authors were able to account for temperature effects and various vehicle speeds, although they considered the same vehicle in all the simulations, i.e., a fixed set of vehicle properties. As an example of practical implementation, smartphones located in regular traffic or public transport can be used to monitor a network of bridges [23–25], i.e., the vehicle fleet does not consist of specialized vehicles fitted with high-end sensors. Preliminary results show promise in terms of smartphones providing enough accuracy for the identification of

frequencies. In this regard, the road profile is known to affect drive-by measurements; thus, its characterization can contribute to the increased accuracy of indirect methods. Keenahan et al. [26] met this task by exploiting the data collected in multiple crossings of a vehicle fleet. Using numerical simulations, the authors were successful in extracting the road profile without prior knowledge of the vehicle properties. A general view of the challenges and opportunities associated with the use of an Intelligent Transport System (ITS) to enhance the performance of SHM systems is provided by Khan et al. [27]. Indirect monitoring in combination with ITS, i.e., traffic cameras and detectors, are presented as a potential precursor for connected vehicle technology, where wireless signals are used to transmit data between vehicles and/or to the bridge infrastructure.

This paper aims to exploit the features contained in the forced response of the first mode of vibration that are not present in free vibration to develop a novel damage detection method. Bridge frequencies associated with the first mode are calculated in forced vibration for each position of a planar 3-axle truck on a bridge beam model using eigenvalue analysis of the coupled system matrix. These calculations cover multiple damage locations and severities, assuming that the damage is modeled as a crack that leads to a loss of bending stiffness at selected elements. Ideally, a relatively large sample of trucks from the operational traffic flow would be employed for gathering information about the bridge. For this reason, the analysis was extended to a truck fleet with a similar static configuration, but differing in dynamic properties. Hence, this method would require the presence of a WIM system onsite for classifying trucks according to their static weights and axle spacing, as well as locating them on the bridge based on their speed. An eigenvalue analysis conducted on a finite element model of the bridge is computationally very fast, and allows a quick picture of the expected impact of damage on the forced frequency pattern of the fleet to be gathered. When carrying out the eigenvalue analysis on a vehicle fleet, it is possible to define probability distributions for the values of the forced frequencies. Moreover, these distributions will change depending on the position of the vehicle and on the location and severity of the damage, hence allowing for the creation of a database. In the absence of field measurements, transient analysis was employed to simulate the acceleration of data collected on the bridge. The transient analysis was performed for a traffic fleet independent from the calibration fleet used in the eigenvalue analysis. The Short-Time Fourier Transform (STFT) was applied to the time-history of accelerations to extract the time-varying frequencies associated with each vehicle crossing. Finally, specific values of the transient forced frequencies were compared to the distributions from eigenvalue analysis to establish whether damage has occurred or not, where, and to what extent. The Mahalanobis distance was used to infer the probability distribution of the database to which a fleet is more likely to belong.

Section 2 describes the research methodology, including the fundamental equations for the VBI model, as well as the main tools used, i.e., STFT and Mahalanobis distance. Section 3 provides details on the specific bridge and traffic fleet models used for testing the methodology. Section 4 illustrates the variation of the forced frequency of the 1st mode of the bridge, and how the probability distribution of forced eigenfrequencies can be obtained from a traffic fleet. Section 5 shows the challenges associated with obtaining the forced frequencies from transient analysis due to the effect of the road profile, vehicle speed, and damping, and how local and global damage affects the forced frequencies. Section 6 presents results for two damage scenarios in two bridge spans traversed by a traffic fleet at two different speeds. Finally, Section 7 draws conclusions and makes suggestions for future research.

## 2. Research Methodology

Damage is seldom localized and quantified considering only the first mode of a structure; it is often necessary to combine this information with data from other modes and dynamic measurements. This paper attempts to overcome this challenge by exploiting the information stored by the time-history of forced frequencies due to a vehicle to estimate

the location and severity of the damage induced by a crack. While this paper uses only the frequency associated with the first mode, it is also making the most out of the unique coupling of a specific vehicle fleet with the first frequency of the bridge for the different positions of the vehicle on the bridge. This section presents the basic steps for implementing the methodology, including the practical aspects, as follows:

- (1) Build a finite element model of the bridge. For this purpose, it is necessary to know the properties of the healthy bridge, which can be obtained based on original drawings and measurements on site to identify the mass ( $[M_b]$ ), stiffness ( $[K_b]$ ) and damping ( $[C_b]$ ) matrices that are involved in the equation of motion of the bridge (Equation (1)).

$$[M_b]\{\ddot{u}_b\} + [C_b]\{\dot{u}_b\} + [K_b]\{u_b\} = \{F_b\} \quad (1)$$

where  $\{u_b\}$ ,  $\{\dot{u}_b\}$  and  $\{\ddot{u}_b\}$  are vectors representing the displacement, velocity and acceleration of the Degrees of Freedom (DoFs) of the bridge, respectively; whereas  $\{F_b\}$  is the vector representing the time-varying forces applied to the bridge.

- (2) Build a multi-body dynamic model of the vehicle representative of the truck fleet. The statistical data for axle spacings and static axle weights of the fleet can be collected from a WIM site near the bridge. In the absence of vehicular measurements, the dynamic properties of the vehicle can be gathered from the literature. Equation (2) represents the equation of motion of the vehicle:

$$[M_v]\{\ddot{u}_v\} + [C_v]\{\dot{u}_v\} + [K_v]\{u_v\} = \{F_v\} \quad (2)$$

where  $[M_v]$ ,  $[K_v]$  and  $[C_v]$  correspond to the mass, stiffness and damping matrices of the vehicle, respectively;  $\{u_v\}$ ,  $\{\dot{u}_v\}$  and  $\{\ddot{u}_v\}$  are vectors representing the displacement, velocity, and acceleration of the DoFs of the vehicle, respectively; and  $\{F_v\}$  is the vector representing the time-varying forces applied to the vehicle.

- (3) Based on steps (1) and (2),  $n$  mass and stiffness matrices are assembled for the coupled vehicle-bridge system for each position of the vehicle on the bridge. VBI modelling is an efficient approach to estimating the bridge response (i.e., forced vibration) due to a moving vehicle, and has been widely used in past research works [28]. It is important to note here that bridge damping is neglected in the current analysis. Also, eigenvalue analysis does not contemplate the road profile, therefore, the methodology is best suited to bridges with very low roughness coefficient.
- (4) Using eigenvalue analysis, the time-history of the first eigenvalue of the coupled vehicle-bridge model is calculated for the  $n$  positions of the vehicle on the healthy bridge. The properties of the vehicle are varied randomly based on typical distributions for the fleet configuration under investigation, i.e., based on statistics from a nearby WIM site. Therefore, each point in the time-history of the first eigenfrequency has a statistical distribution associated with it. Equation (3) shows the eigenvalue analysis for a given position  $i$  over the bridge of the vehicle with a set of properties  $j$ .

$$\left| [M_g]^{-1} [K_g^{i,j}] - \alpha I_g \right| = 0 \text{ with } i \in [1, n] \text{ and } j \in [1, s] \quad (3)$$

where  $[M_g]^{-1}$  represents the inverse of the coupled mass matrix, which is independent of the position of the vehicle;  $[K_g^{i,j}]$  corresponds to the coupled stiffness matrix when a vehicle with a set of properties  $j$  is located at position  $i$  over the bridge;  $\alpha$  is the vector of eigenvalues and  $I_g$ , the identity matrix. Finally,  $s$  represents the size of the fleet considered in the eigenvalue analysis. By solving Equation (3) for each value of  $i$  and  $j$  and keeping the first element of  $\alpha$ , it is possible to obtain  $n$  vectors of  $s$  components that characterize the statistical distribution of the first forced

eigenfrequency of the healthy bridge at each vehicle location for the selected fleet configuration.

- (5) The process described in step (4) is repeated here for a wide range of damage scenarios. In addition to varying the properties of the vehicle based on typical values for the fleet configuration, the stiffness of the bridge is varied according to the parameters of a damage model (i.e., crack location and severity). A specific set of parameters of the damage model leads to a specific set of statistical distributions of the first frequency for each location of the vehicle on the bridge. Experimental data for the development of damage models is limited mostly to beams tested in a lab, and there is a large degree of uncertainty surrounding existing damage or its evolution for a complex structure. For example, the true shape of an existing loss of bending stiffness associated with a particular damage location in a bridge (i.e., a crack) and the assumed mathematical model to characterize a similar damage at the same location may differ considerably. If the width of the shape is narrower in reality than in the mathematical model, then the methodology will be prone to underestimate the depth. Overall, it is expected that small changes in the shape would affect mainly the higher frequencies of the bridge, whereas the first frequency would only change to a small extent. Thus, predictions from the proposed methodology should still be able to point a bridge inspector in the right direction.
- (6) The acceleration response of the bridge is measured for  $p$  crossings of random trucks within the selected fleet configuration. The latter entails the availability of a WIM system immediately before or after the bridge to identify those trucks that belong to the fleet. Here, the method is tested with theoretical accelerations due to the unavailability of field tests. The interaction between the vehicle and the bridge is implemented using MATLAB R2022a [29]. Therefore, the acceleration response is simulated by integrating the equations of motion of the coupled VBI system defined in Equation (4).

$$[M_g]\{\ddot{u}_g\} + [C_g]\{\dot{u}_g\} + [K_g]\{u_g\} = \{F_g\} \quad (4)$$

where  $[M_g]$ ,  $[C_g]$ , and  $[K_g]$  represent the global mass matrix, global damping matrix, and global stiffness matrix, respectively;  $\{F_g\}$  is the global force vector; and  $\{u_g\}$  is the unknown displacement vector. The symbols  $\dot{\phantom{x}}$  and  $\ddot{\phantom{x}}$  indicate the first and second derivative with respect to time, respectively. The Newmark-beta integration approach (with  $\gamma = 0.5$  and  $\beta = 0.25$ ) is used to obtain the bridge response, and more specifically, the acceleration of the mid-span section. Details about the integration are referred to González [28].

- (7) The STFT of the acceleration response is calculated for each of the  $p$  crossings, as per Equation (5). It should be noted that other signal processing tools can potentially be used instead of the STFT here to obtain the time-frequency representation of the acceleration signal, i.e., Hilbert Huang Transform [30], wavelets [31], etc.

$$STFT\{\ddot{u}_g(t)\}(\tau, \omega) = \int_{-\infty}^{\infty} \ddot{u}_g(t)w(t - \tau)e^{-i\omega t} dt \quad (5)$$

where  $\ddot{u}_g(t)$  represents the acceleration signal,  $w(\tau)$  is the window function and  $\omega$  corresponds to the frequency. Acceleration signals of short duration will lead to a poor frequency resolution. Therefore, the methodology will perform best with a longer duration of the signal. An ideal scenario would consist of a long vehicle crossing a long bridge at low speed, with speed having the greatest impact on accuracy. In practice, the latter limits the range of application to bridges where speed restrictions apply, i.e., located in an urban area, or close to a junction where a vehicle must slow down. Initially, the bridge can be assumed to be healthy, and the mean

pattern of forced vibrations obtained here can be used to calibrate the VBI model proposed in step (4).

- (8) For every vehicle crossing, a set of frequency values is selected within the time-history of forced frequencies. These values of frequencies correspond to the same specific locations of the vehicle over the bridge. It is essential to choose locations where the frequency estimation is not hindered by edge effects derived from the application of the signal processing tool. In this paper, the methodology is tested using only two vehicle positions ( $i_1, i_2$ ) and two frequencies, but it could be potentially extended to include more positions over the bridge.
- (9) As a result of steps (1) to (5), a database of bivariate distributions of the eigenfrequency values corresponding to the healthy bridge and each damage scenario is generated based on the frequencies corresponding to the two selected vehicle positions. Alternatively, a multivariate distribution of higher order would be employed in case of selecting more than two values from the time-history of forced frequencies. Then, Equation (6) is applied to obtain the Mahalanobis distance [32,33],  $MD_r^q$ , between the points defined by the frequencies in the  $q = 1, 2, 3, \dots, p$  vehicle crossings and the statistical distributions obtained using eigenvalue analysis (steps (4) and (5)).

$$MD_r^q = \sqrt{\{y^q - \bar{\mu}_r\}^T [S_r]^{-1} \{y^q - \bar{\mu}_r\}} \quad r = 1, 2, 3, \dots, R \quad (6)$$

where  $r$  represents a distribution from the eigenvalue database,  $R$  is the total number of the bivariate distributions, and  $\bar{\mu}_r$  and  $[S_r]$  denote the sample mean and covariance of the reference bivariate distribution, respectively.  $[S_r]$  is a square matrix with an order equal to the number of selected forced frequencies. For each vehicle crossing, there is an observation  $\{y^q\}$  (i.e., set of selected forced frequencies) which is used to measure the Mahalanobis distance between the observation and the reference bivariate distribution. The superscripts  $^T$  and  $^{-1}$  indicate the transpose of a vector and inverse of a matrix, respectively.

- (10) For vehicle crossing  $q = 1$ , it is possible to calculate  $MD_1^1, MD_2^1, MD_3^1, \dots, MD_R^1$  according to Equation (6). If there are  $p$  vehicle crossings, a mean Mahalanobis distance is defined for each distribution  $r$  as follows:  $\overline{MD}_r = \sum_{q=1}^p \frac{MD_r^q}{p}$ . The  $R$  distributions are ranked in ascending order according to the mean Mahalanobis distance  $\overline{MD}_r$ . The location and severity associated with the statistical distribution yielding the lowest value of the mean Mahalanobis distance are used to estimate the damage. The Mahalanobis distance can be employed to assist in the selection of the frequencies in step (8). It is found that, generally, combinations of frequencies leading to high values of the Mahalanobis distance will yield more inaccurate results than combinations with low values of the distance.

### 3. Vehicle-Bridge Interaction Model

#### 3.1. Bridge Model

A 15 m span bridge is modeled as a simply supported Euler-Bernoulli beam discretized into 150 elements 0.1 m long each. Hence, there are 151 nodes in total with 2 DoFs per node, representing the vertical translation and in-plane rotation of each node. The elementary mass  $[M_e]$  and stiffness  $[K_e]$  matrices are expressed in Equations (7) and (8), respectively.

$$[M_e] = \frac{mL_e}{420} \begin{bmatrix} 156 & 22L_e & 54 & -13L_e \\ 22L_e & 4L_e^2 & 13L_e & -3L_e^2 \\ 54 & 13L_e & 156 & -22L_e \\ -13L_e & -3L_e^2 & -22L_e & 4L_e^2 \end{bmatrix} \quad (7)$$

$$[K_e] = \frac{EI}{L_e^3} \begin{bmatrix} 12 & 6L_e & -12 & 6L_e \\ 6L_e & 4L_e^2 & -6L_e & 2L_e^2 \\ -12 & -6L_e & 12 & -6L_e \\ 6L_e & 2L_e^2 & -6L_e & 4L_e^2 \end{bmatrix} \quad (8)$$

where  $m$ ,  $L_e$ ,  $E$ , and  $I$ , represent the mass per unit length, length of each element, modulus of elasticity and moment of area, respectively. The vertical translation of the left end node and its associated rotation are represented by the 1st and 2nd rows of the matrices in Equations (7) and (8), and similarly for the right end node by the 3rd and 4th rows. By assembling all the elementary mass and stiffness matrices, it is possible to obtain the bridge mass and stiffness matrices used in Equation (1). The dimensions of these matrices are  $302 \times 302$  in this paper.

Table 1 summarizes the values of the bridge properties, based on a reinforced concrete solid slab with a constant cross-section [34,35].

**Table 1.** Parameters of the bridge model.

Parameter	Value	Unit
Length, $L_b$	15	m
Width, $w$	15	m
Depth, $h$	0.75	m
Mass per unit length, $m$	28,125	kg/m
Modulus of elasticity, $E$	$35 \times 10^9$	Pa
Second moment of area, $I$	0.5273	m <sup>4</sup>

The first three frequencies associated with the longitudinal modes of vibration of the bridge are 5.655 Hz, 22.622 Hz, and 50.900 Hz. These values are consistent with the literature [36,37], in terms of the relationship between the bridge fundamental frequency and its span length, i.e., approximately  $85/L_b$  for the first frequency of a 15 m concrete bridge. Damping is usually low in bridges, and it is neglected in this paper unless otherwise specified. For instance, Castellanos-Toro et al. [38] report that nearly 60% of the damping ratios of vehicular and pedestrian bridges fall within the 1–5% range, with the majority of values concentrated around a value of 3% for vertical frequencies.

Sinha et al. [39] propose a linear stiffness reduction as an approximation of the exponential function developed by Christides and Barr [40] for modeling the decay in stiffness due to a crack in steel beams. A different non-linear function is available to model the stiffness loss due to a crack in reinforced concrete beams [41], and it has been used by other authors in the context of moving vehicular loads [42]. For simplification purposes, the linear approximation by Sinha et al. is applied here to represent the stiffness loss in a reinforced concrete bridge. The damage severity of the crack, typically labeled as  $\lambda$ , is defined by the ratio of the crack depth to the total beam depth. The crack is assumed to extend across the width of the entire section. If the total beam depth is  $h$ , stiffness increases linearly from a minimum at the crack location to a maximum (healthy condition, i.e., 0.5273 m<sup>4</sup>) at a distance of  $1.5h$  (Figure 1). If  $h = 0.75$  m and  $\lambda = 15\%$ , the crack has a depth of 11.25 cm and the relative stiffness loss in percentage at the cracked section is approximately  $(1 - (1 - 0.15)^3) \times 100 = 38.59\%$  based on a rectangular cross-section. For  $\lambda = 5\%$ , the crack depth is 3.75 cm and the relative stiffness loss is 14.26%.



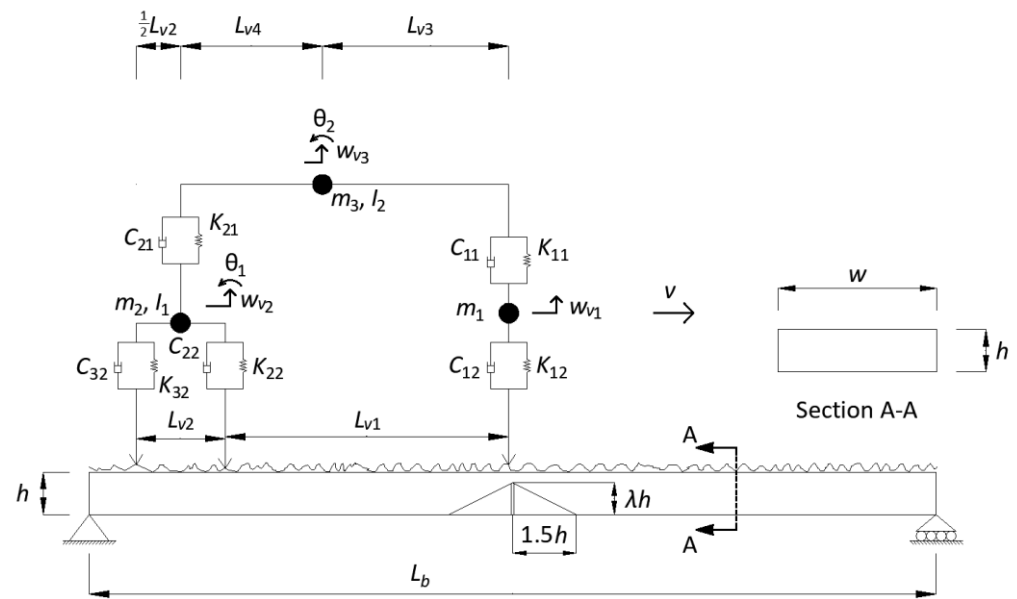


Figure 1. Vehicle-bridge interaction model.

### 3.2. Vehicle Model

Figure 1 depicts the planar 3-axle rigid truck model employed in the simulations.

The truck model has 5 DoFs, namely the vertical displacements of the front axle, rear tandem and body masses (labeled in the figure as  $w_{v1}$ ,  $w_{v2}$  and  $w_{v3}$ , respectively) and the rotations of the rear tandem mass ( $\theta_1$ ) and the body mass ( $\theta_2$ ). The mass  $[M_v]$ , damping  $[C_v]$ , and stiffness  $[K_v]$  matrices used in Equation (2) are given in Equations (9)–(11).

$$[M_v] = \begin{bmatrix} m_1 & 0 & 0 & 0 & 0 \\ 0 & m_2 & 0 & 0 & 0 \\ 0 & 0 & I_1 & 0 & 0 \\ 0 & 0 & 0 & m_3 & 0 \\ 0 & 0 & 0 & 0 & I_2 \end{bmatrix} \quad (9)$$

$$[C_v] = \begin{bmatrix} C_{11} + C_{12} & 0 & 0 & -C_{11} & C_{11}L_{v3} \\ 0 & C_{21} + C_{22} + C_{32} & \frac{(-C_{22} + C_{32})L_{v2}}{2} & -C_{21} & -C_{21}L_{v4} \\ 0 & \frac{(-C_{22} + C_{32})L_{v2}}{2} & \frac{(C_{22} + C_{32})L_{v2}^2}{4} & 0 & 0 \\ -C_{11} & -C_{21} & 0 & C_{11} + C_{21} & -C_{11}L_{v3} + C_{21}L_{v4} \\ C_{11}L_{v3} & -C_{21}L_{v4} & 0 & -C_{11}L_{v3} + C_{21}L_{v4} & C_{11}L_{v3}^2 + C_{21}L_{v4}^2 \end{bmatrix} \quad (10)$$

$$[K_v] = \begin{bmatrix} K_{11} + K_{12} & 0 & 0 & -K_{11} & K_{11}L_{v3} \\ 0 & K_{21} + K_{22} + K_{32} & \frac{(-K_{22} + K_{32})L_{v2}}{2} & -K_{21} & -K_{21}L_{v4} \\ 0 & \frac{(-K_{22} + K_{32})L_{v2}}{2} & \frac{(K_{22} + K_{32})L_{v2}^2}{4} & 0 & 0 \\ -K_{11} & -K_{21} & 0 & K_{11} + K_{21} & -K_{11}L_{v3} + K_{21}L_{v4} \\ K_{11}L_{v3} & -K_{21}L_{v4} & 0 & -K_{11}L_{v3} + K_{21}L_{v4} & K_{11}L_{v3}^2 + K_{21}L_{v4}^2 \end{bmatrix} \quad (11)$$

where  $C_{ij}$  represents the damping values;  $K_{ij}$ , stiffness values;  $L_{vi}$ , distances;  $m_i$ , masses; and  $I_i$ , mass inertias of the vehicle.

Table 2 lists typical values of properties for a 3-axle truck, calibrated experimentally [8,43]. These values are assumed to be the mean values for a truck fleet that will be defined further on. An eigenvalue analysis led to five vehicle frequencies, 2.153, 2.671, 14.806, 15.572 and 15.827 Hz, representing the body mass bounce, the body mass pitch, the rear axle pitch, the front axle hop and the rear axle hop, respectively.

**Table 2.** Parameters of the vehicle model.

Parameter	Value	Unit
Geometry		
Spacing between front and 1st rear axle, $L_{v1}$	5.40	m
Spacing between 1st and 2nd rear axle, $L_{v2}$	1.20	m
Distance between $m_1$ and $m_3$ , $L_{v3}$	4.40	m
Distance between $m_2$ and $m_3$ , $L_{v4}$	1.60	m
Weights		
Gross Vehicle Weight, $GVW$	241.00	kN
Front axle, $P_1$	64.11	kN
1st Rear axle, $P_2$	88.45	kN
2nd Rear axle, $P_3$	88.45	kN
Masses		
Front axle unsprung, $m_1$	500	kg
Rear tandem unsprung, $m_2$	1450	kg
Body sprung, $m_3$	22,625	kg
Mass moments of inertia		
Rear tandem unsprung mass, $I_1$	732	kg·m <sup>2</sup>
Body sprung mass, $I_2$	162,162	kg·m <sup>2</sup>
Spring stiffness		
Front suspension, $K_{11}$	1577	kN/m
Rear suspension, $K_{21}$	4724	kN/m
Front tire, $K_{12}$	3146	kN/m
Rear tires, $K_{22}$ , $K_{32}$	4724	kN/m
Damping coefficients		
Front suspension, $C_{11}$	22.40	kN·s/m
Rear suspension, $C_{21}$	66.84	kN·s/m
Front tire, $C_{12}$	13.30	kN·s/m
Rear tires, $C_{22}$ , $C_{32}$	10.00	kN·s/m

### 3.3. Truck Fleet

The parameters for the truck fleet were generated based on the normal distributions defined in Table 3. The mean and standard deviation of the distributions for the static mechanical parameters in Table 3 (i.e., geometry and weights) are based on histograms of WIM data recorded in a motorway in Auxerre, France [44]. Particularly, Table 3 adopts the values of the normal distribution fitted to the peak of the histogram associated with fully loaded 3-axle trucks, in line with common WIM practice. Additionally, the mean values of the rest of the parameters in Table 3 (i.e., mass, spring stiffness, damping coefficient) were taken from the literature [43], and their corresponding standard deviations are based on Cantero et al. [45]. It is worth mentioning that some other vehicle design standards [46] and road safety guidelines [47] are taken into consideration to have reasonable minimum and maximum values. In other words, the distributions are truncated to ensure that a realistic range of values will be sampled.

**Table 3.** Statistical distributions of vehicle parameters for the truck fleet.

Parameter	Mean	STD	Min	Max
Geometry (m)				
$L_{v1}$	5.4	0.2	5.2	5.6
$L_{v2}$	1.2	0.2	1.1	1.3
Weights				
$GVW$ (kN)	241	57.5	183.5	299

$W_1(\%)$ (*)	26.6	2.1	24.5	28.7
Masses (kg)				
$m_1$	500	50	400	600
$m_2$	1450	145	1160	1740
Spring stiffness (kN/m)				
$K_{11}$	1577	236.55	1103.9	2050.1
$K_{21}$	4724	1181	2362	7086
$K_{12}$	3146	786.5	1573	4719
$K_{22}, K_{32}$	4724	1181	2362	7086
Damping coefficients (kN·s/m)				
$C_{11}$	22.40	6.72	8.96	35.84
$C_{21}$	66.84	20.05	26.74	106.94
$C_{12}$	13.30	3.99	5.32	21.28
$C_{22}, C_{32}$	10.00	3.00	4.00	16.00

(\*)  $W_1$  represents  $P_1$  from Table 1 as a% of  $GVW$ .

The Monte Carlo method was used to randomly sample values from the distributions in Table 3. As a result, a fleet composed of  $s = 1000$  different trucks was generated. Figure 2 shows the histogram of frequencies associated with the first five modes of vibration of the 1000 vehicles. There is reasonable agreement between the histogram of frequencies and the past research by Cebon [48] and White [49], i.e., frequencies for the body mass bounce and pitch vary between 1.5 and 3 Hz (as Figure 2a,b), and frequencies for the rear tandem hop and pitch and the front axle hop are found between 7 and 20 Hz (as Figure 2c–e).

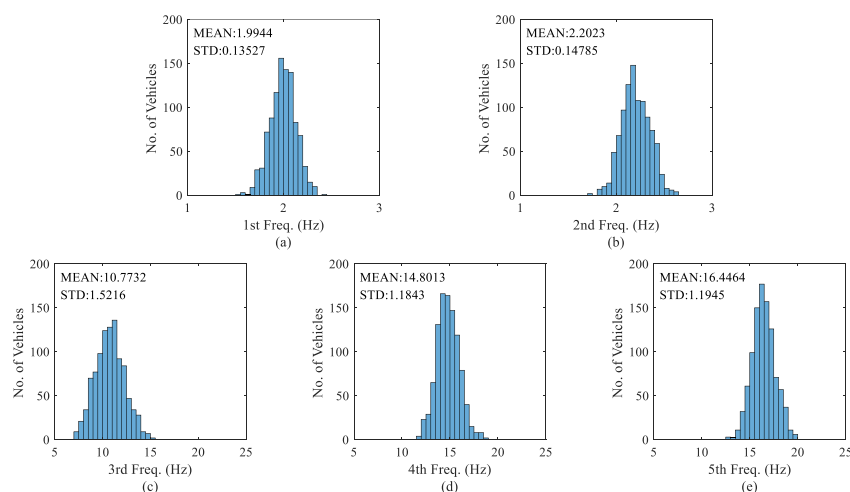


**Figure 2.** Histogram of frequencies of vibration of the fleet for: (a) the 1st mode, (b) the 2nd mode, (c) the 3rd mode, (d) the 4th mode, and (e) the 5th mode of vibration.

## 4. Eigenvalue Analysis

### 4.1. Healthy Bridge

Figure 3 shows the first bridge eigenfrequency versus the location of the front axle of the vehicle for a healthy version of the bridge, obtained as described in steps (1) to (4) of the methodology presented in Section 2. The value of the eigenfrequency corresponding to a truck based on the mean values of Table 2 is represented by a black solid curve. The red dash-dotted and blue dashed curves correspond to the values of mean and mean  $\pm$  standard deviation, respectively, of the 1000 eigenfrequencies obtained for each position of the fleet (Section 3.3) on the bridge. The black solid and red dash-dotted curves become

closer as the size of the sample increases, being a reasonable match for the 1000 trucks calibration sample.

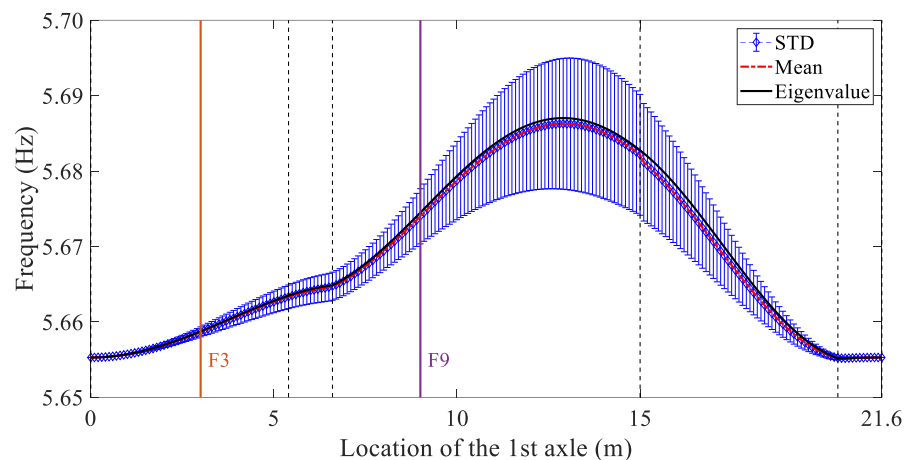
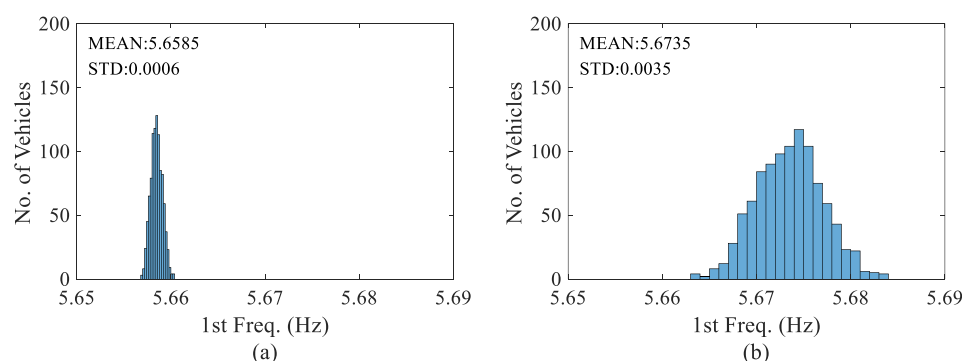


**Figure 3.** Bridge eigenfrequencies vs. location of the 1st axle on the bridge.

In Figure 3, there are four vertical dashed lines indicating the 2nd and 3rd axles entering the bridge (5.4 and 6.6 m) and the 1st and 2nd axles leaving the bridge (15 and 20.4 m). Vertical solid lines signal the frequency  $F_3$ , associated with the 1st axle located at 3 m and the frequency  $F_9$  associated with the 1st axle at 9 m. The selected locations at 3 and at 9 m seek a compromise between a low sensitivity to the variability of the fleet, and a relatively far distance from singularities associated with the entrance and exit of axles. The values of the eigenfrequencies at these two locations ( $F_3$  and  $F_9$ ) will be used as references in subsequent analyses.

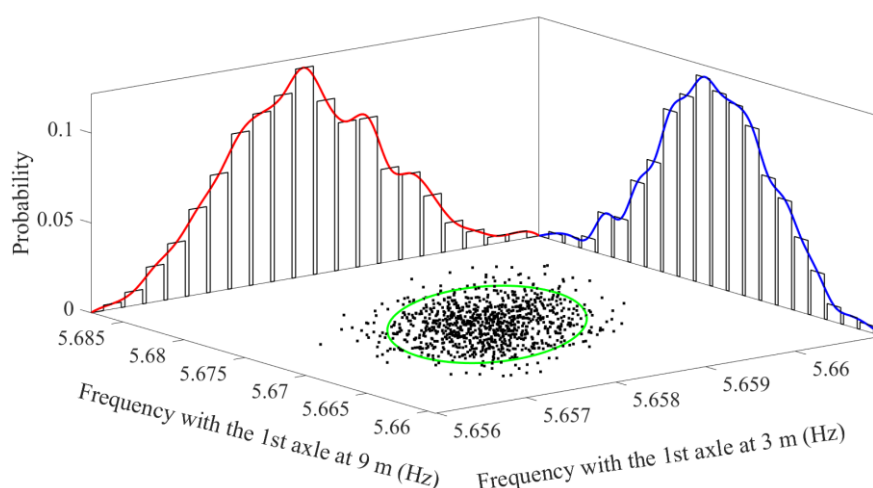
It is noted that the standard deviation increases significantly after the 3rd axle of the vehicle enters the bridge ( $x = 6.6$  m), and it decreases when the 1st axle is about to leave the bridge ( $x = 15$  m). The eigenfrequencies for locations between 10 and 15 m are most sensitive to the variability of the truck fleet. The use of frequencies in this 10–15 m range would only be advisable in the case of having a large fleet available for testing, in order to get a good approximation of the mean value. It is worth mentioning that the variability displayed in Figure 3 belongs to a general population of 3-axle trucks, but could be further reduced by limiting the characteristics of the fleet. For example, the fleet was generated by sampling axle weights and axle spacings of a 3-axle truck randomly based on normal distributions from real WIM data as per Table 3. However, a WIM or BWIM system would allow measuring these static properties to narrow down on a subset of the general 3-axle truck fleet that could be used to derive a more specific Figure 3. Although some variability will remain as a result of the uncertainty on the dynamic properties of the subset, this uncertainty would be considerably smaller than when also covering for the static properties.

Figure 4a,b show the number of vehicles versus the bridge eigenfrequencies ( $F_3$  and  $F_9$ ) for locations  $x = 3$  m and  $x = 9$  m, respectively. The histogram of eigenfrequencies appears to follow a normal distribution with a mean value of 5.658 Hz and a standard deviation of 0.0006 Hz for  $F_3$ , and with a mean value of 5.673 Hz and a standard deviation of 0.0035 Hz for  $F_9$ . In agreement with the discussion above, the uncertainty around  $F_9$  is clearly larger than for  $F_3$ .



**Figure 4.** No. vehicles versus bridge eigenfrequencies associated with the 1st axle located at: (a) 3 m and (b) 9 m, from 1st support.

A bivariate distribution can be fitted to the 1000  $F_3$  eigenfrequencies and 1000  $F_9$  eigenfrequencies as per Figure 5. Here, the  $x$ -axis represents the individual distribution of  $F_3$  highlighted in red, the  $y$ -axis represents the individual distribution of  $F_9$  highlighted in blue, and the  $z$ -axis represents the probability. The ellipse highlighted in green is based on the individual mean and standard deviations of  $F_3$  and  $F_9$ . This ellipse contains 86.6% of all combinations of  $F_3$  and  $F_9$  inside its perimeter, i.e., 866 trucks.



**Figure 5.** Bivariate distribution of bridge eigenfrequencies associated with the 1st axle located at 3 and at 9 m.

#### 4.2. Damaged Bridge

If different crack locations and severities are introduced in the coupled VBI finite element model, the values of the eigenfrequencies in Figures 3–5 will change. Figure 6 illustrates the result of adjusting a bivariate normal distribution to  $F_3$  and  $F_9$  for the same bridge and truck fleet, but with different damage scenarios (step (5) in Section 2). This is the database mentioned in step (9) of the methodology that will be used for comparison to the frequencies extracted from the acceleration signal. Only damage locations in the first half of the bridge (up to 7.5 m from the left support) are considered here. The ellipses in the figure represent the frequency distributions with 86.6% probability. Ellipses drawn with thick solid lines, dotted lines, and dashed lines represent cracks with  $\lambda = 5\%$ ,  $\lambda = 10\%$ , and  $\lambda = 15\%$  respectively. It can be seen that the distributions align along a straight line approximately. For the same crack location, deeper cracks lead to lower frequencies. As expected, the distribution for the healthy beam, in solid thick black, is located in the upper right corner of the figure. For the same crack severity ( $\lambda$ ), the 1st bridge frequency

tends to decrease as the crack location becomes closer to the mid-span of the bridge. For the smaller values of damage severity, ellipses are more closely spaced.

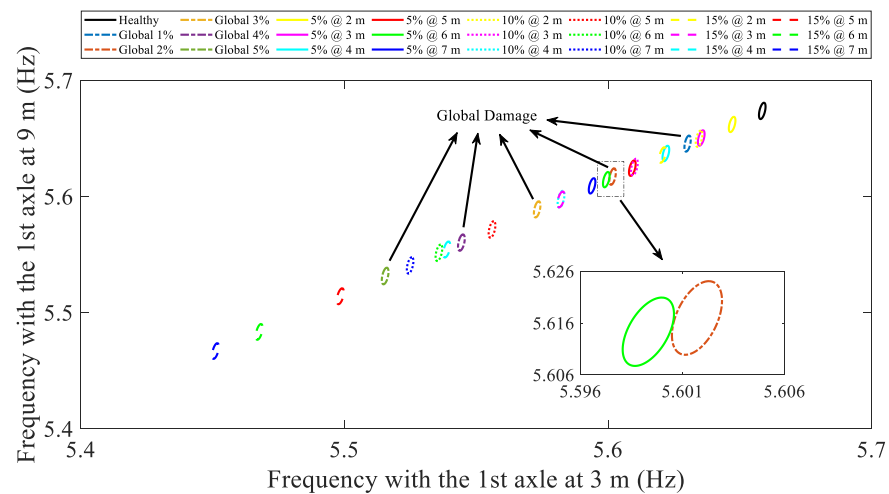


**Figure 6.** Bivariate distributions of bridge eigenfrequencies at 3 m and 9 m associated with a healthy bridge, 18 local stiffness losses (six different damage locations and three damage severities) and 5 global stiffness losses.

In addition to the local stiffness losses defined by Sinha et al. [39] (Section 3.1), five global stiffness losses are also considered. Global stiffness loss is defined as a percentage (1%, 2%, 3%, 4% and 5%) of the healthy bridge stiffness (i.e.,  $18.4555 \times 10^9$  N/m<sup>2</sup>). The five bivariate distributions representative of a potential global damage are highlighted in Figure 6 as dash-dotted ellipses. It must be emphasized that global stiffness losses are not necessarily related to damage, but to environmental causes such as changes in temperature and humidity [50]. Hence, environmental conditions have to be monitored together with the frequencies. Figure 6 shows that the forced-frequencies due to local and global changes follow a similar pattern. A zoom onto two distributions next to each other, one local (green solid) and another global (orange dash-dotted), distinguishes small differences in their shapes, i.e., the global ellipse is larger than the local ellipse due to a higher value of the standard deviation for  $F_9$ .

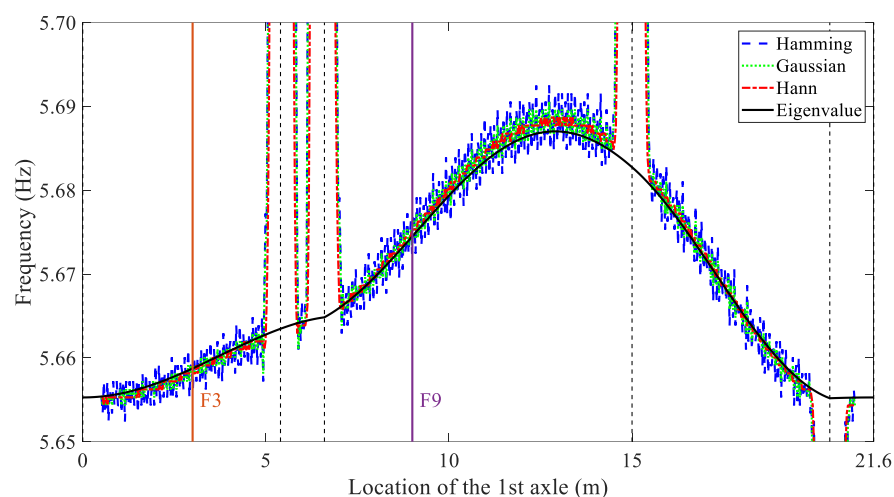
## 5. Transient Analysis

The dynamic transient analysis aims to simulate the response that would be measured in the field. The coupled equations of motion of the VBI system are integrated to obtain a time series of the acceleration response at midspan due to the passing of the vehicle at a constant speed of 1 m/s. The very low selected speed has the purpose of assessing differences with eigenvalue analysis in the absence of other factors, such as the duration of the signal or edge effects. The STFT is employed to extract the time history of forced frequencies.

### 5.1. Healthy Bridge

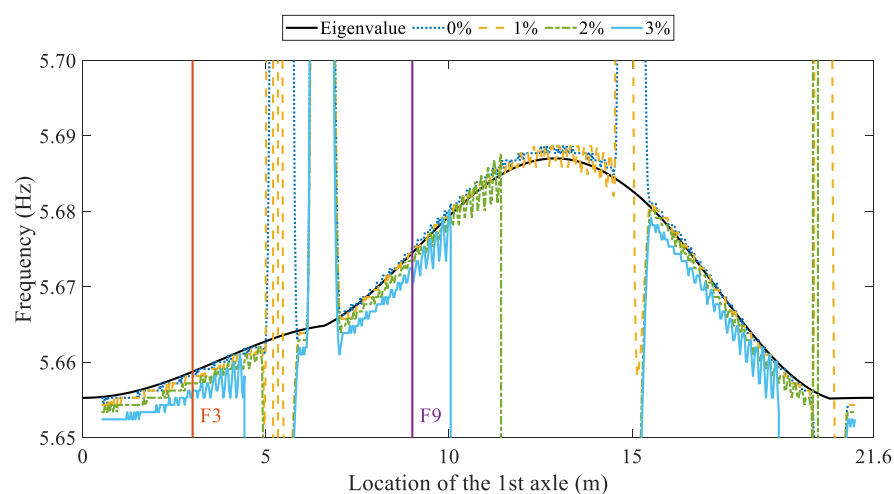
There are various window function types that can be utilized in the STFT for instantaneous frequency extraction; the Hamming, Gaussian and Hann are amongst the most popular options [51]. Figure 7 shows the difference between these windows compared to the eigenvalue analysis for the vehicle given in Section 3.2. The Hann window outperforms the other two alternatives when intending to match the eigenvalue curve. In order to optimize the trade-off between time and frequency resolution [52], the selected length for the Hann window is  $2^{10}$ , the hop size is  $2^5$  and the total number of fast Fourier transform (FFT) points is  $2^{20}$ . Figure 7 shows how the entrances and exits of the axles induce

significant deviations between the eigenfrequencies and the instantaneous frequencies due to edge effects. The locations for capturing the frequencies  $F_3$  and  $F_9$  were selected to avoid these “blind spots”.



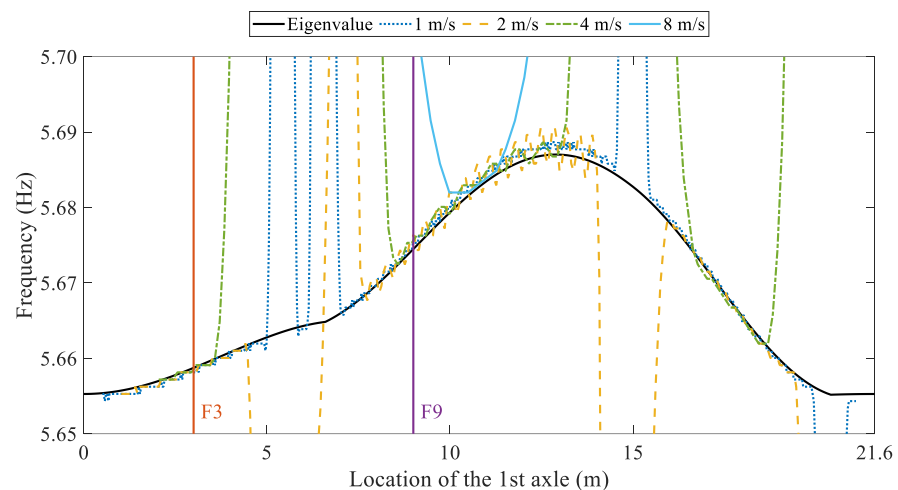
**Figure 7.** Comparison of the eigenvalue curve and the STFT of the undamped bridge response due to the truck travelling at 1 m/s on a smooth profile using three different window functions.

Figure 8 compares the effect of damping on the instantaneous forced frequency obtained from the bridge acceleration due to the same truck (Section 3.2) traveling at 1 m/s. Classical Rayleigh damping is employed here to model viscous damping on the bridge as a linear combination of the mass and stiffness matrices [53]. There are two constants related to the Rayleigh damping, pre-multiplying mass and stiffness matrices, defined as:  $\alpha_R = 2\xi\omega_1\omega_2/(\omega_1 + \omega_2)$ , and  $\beta_R = 2\xi/(\omega_1 + \omega_2)$ , respectively, where  $\omega_1$  and  $\omega_2$  are the first two angular frequencies of the bridge. The damped frequency,  $f_d$ , is defined by  $f\sqrt{1 - \xi^2}$  [54], where  $f$  is the undamped frequency and  $\xi$  is the damping ratio. As the modal damping increases, the damped frequency decreases, but only slightly, given the low damping found in bridges. Values of  $\xi = 1\%$ ,  $2\%$  and  $3\%$  in the figure do not show a significant deviation from the  $0\%$  damping adopted in this paper.



**Figure 8.** Comparison of the eigenvalue curve and the STFT of the bridge response due to the truck traveling at 1 m/s on a smooth profile for four bridge damping ratios.

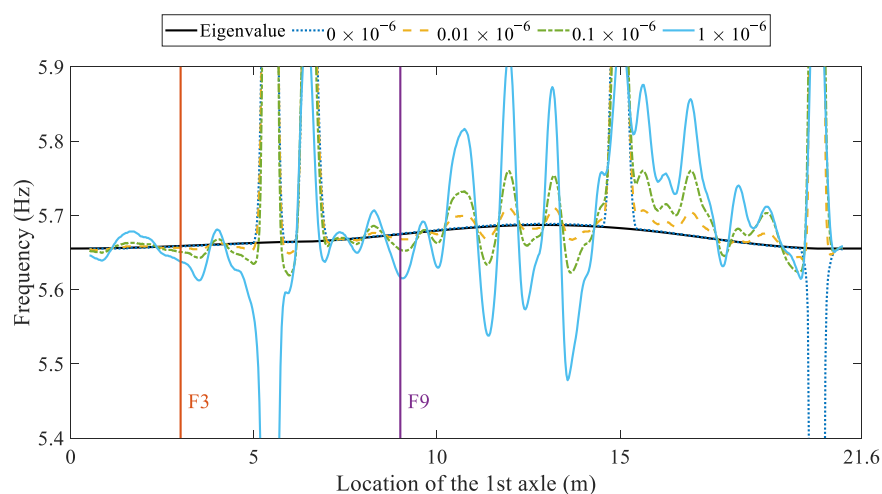
Figure 9 shows the history of forced frequencies for four different vehicle speeds, namely 1 m/s, 2 m/s, 4 m/s and 8 m/s. The STFT at 1 m/s offers the most reliable results regardless of the axle location. Although a higher speed could be employed, there are limitations related to a worsening of the frequency resolution, and to the contamination of the STFT by wider and more pronounced edge effects. Therefore, extreme caution should be placed in the selection of the vehicle positions when employing high vehicle speeds. For the two locations selected in the paper, i.e.,  $F_3$  and  $F_9$ , the STFT of the mid-span acceleration when the vehicle travels at 4 m/s is still able to provide accurate results. However, the STFT at 8 m/s resembles the eigenvalue curve only for a small portion between 10 and 11 m. It should be pointed out that a bridge span longer than the 15 m investigated here would potentially allow for higher speeds to be implemented. Firstly, a longer span captures a longer duration of the measurements, and, consequently, leads to a better frequency resolution. Secondly, the interference of axles entering and leaving the bridge that corrupts the forced vibration record will have a comparatively lesser impact.



**Figure 9.** Comparison of the eigenvalue curve and the STFT of the undamped bridge response due to the truck travelling on a smooth profile at four different speeds.

The simulations conducted in this paper adopt a smooth road profile. Figure 10 shows the impact of increasing the roughness coefficient of the road, i.e., the geometric spatial mean in  $\text{m}^3/\text{cycle}$ . The road profile was generated through an inverse FFT of its power spectral density function based on the usual assumption of being a zero-mean stationary Gaussian random process [55]. Although the tested three roughness coefficients ( $0.01 \times 10^{-6}$ ,  $0.1 \times 10^{-6}$ ,  $1 \times 10^{-6}$ ,  $\text{m}^3/\text{cycle}$ ) correspond to a ‘very good’ profile (Class ‘A’ according to ISO standards [56]), the overall pattern, and more specifically the values of  $F_3$  and  $F_9$ , rapidly deviate from the eigenvalue curve.

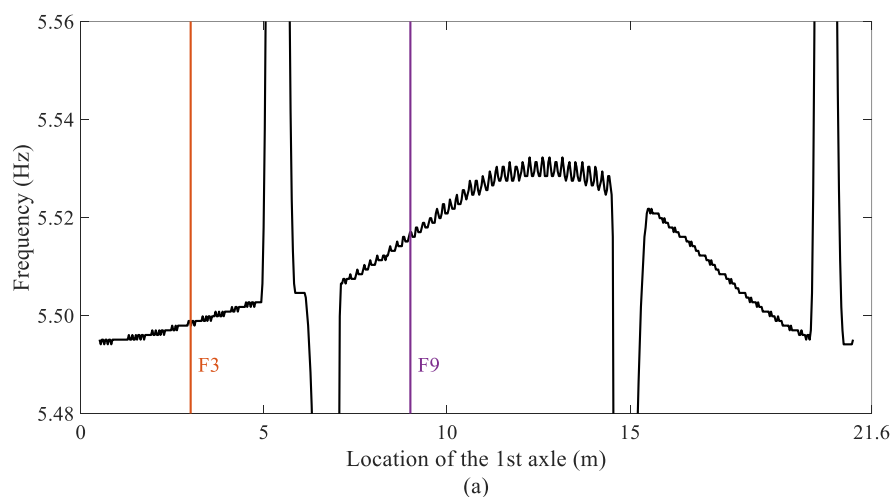




**Figure 10.** Comparison of the eigenvalue curve and the STFT of the undamped bridge response due to the truck travelling at 1 m/s on four roads with different roughness coefficients.

### 5.2. Damaged Bridge

Figure 11a shows the instantaneous frequencies of a bridge in a damage scenario ‘A’ with a 15% crack at 5 m, using the truck of Section 3.2. The latter is assumed to be representative of a large fleet of 3-axle configurations. In this investigation, only the values of  $F_3$  and  $F_9$ , marked in the figure with two vertical solid lines, were retained for further analysis. Figure 11b is the equivalent of Figure 11a for damage scenario ‘B’ with a smaller crack (only 5% of the depth of the beam) located at 7 m. As expected, the changes in eigenfrequencies for damage ‘B’ with respect to the healthy condition (Figure 3) are significantly smaller than for damage ‘A’.



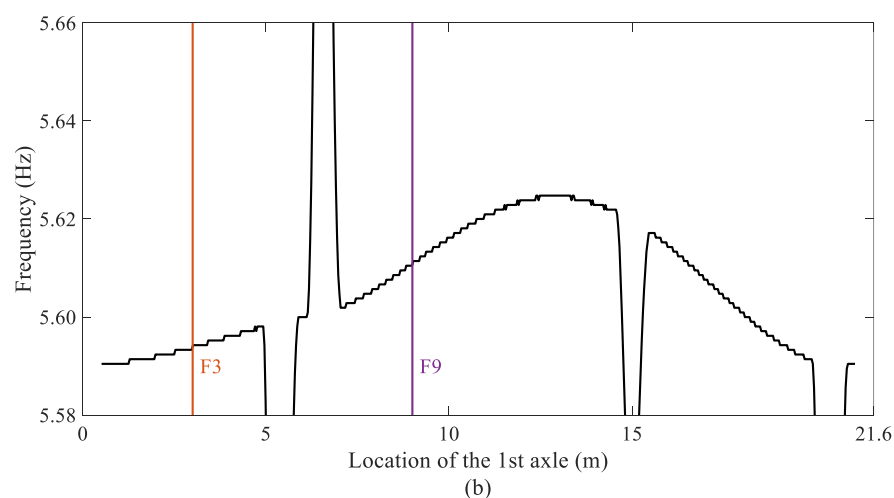
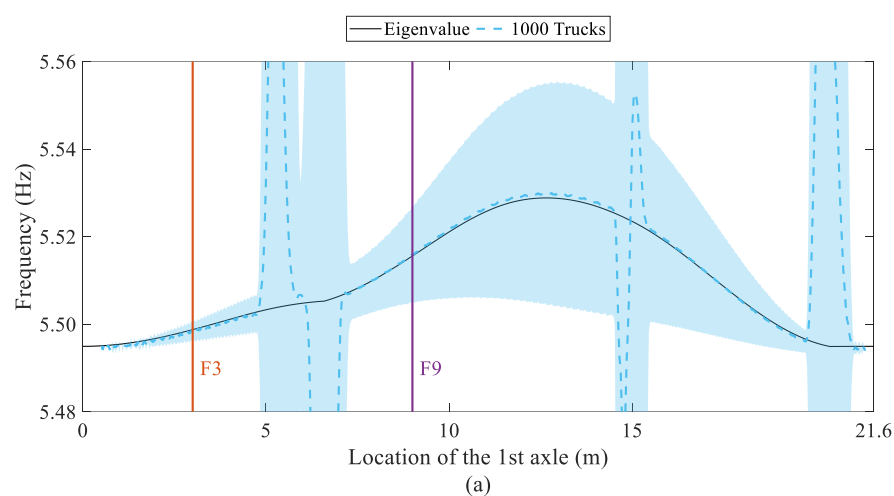


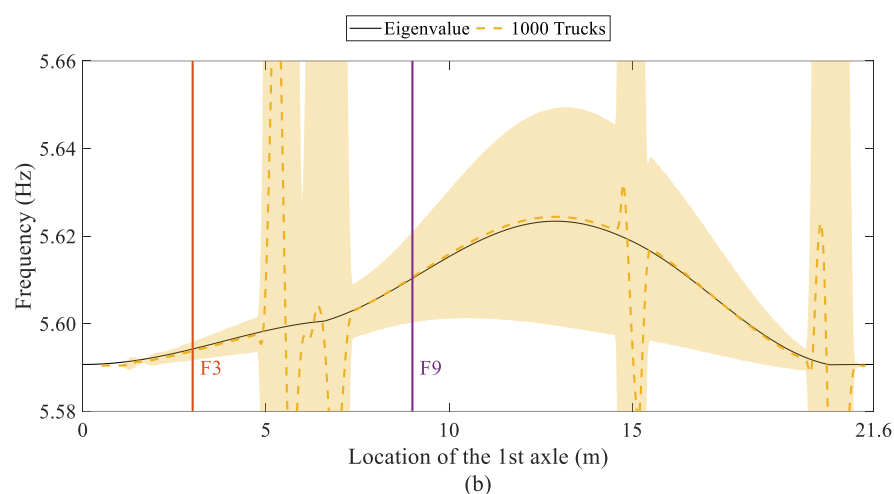
**Figure 11.** Instantaneous frequencies by STFT vs. location of the 1st axle for scenarios: (a) 15% crack at 5 m, and (b) 5% crack at 7 m.

## 6. Discussion

### 6.1. Testing of a 15 m Bridge

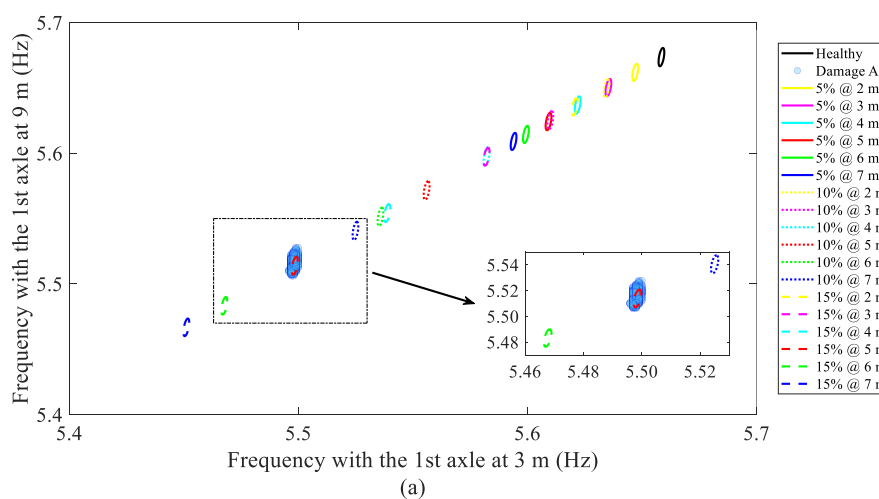
This section shows how eigenvalue analysis can be exploited to locate and quantify damage based on the changes in the forced frequencies  $F_3$  and  $F_9$ . For this purpose, Figure 12 compares the forced frequencies of a fleet composed of  $p = 1000$  3-axle trucks to the associated eigenfrequencies for two damage scenarios. The forced frequency versus vehicle position for a 15% crack at 5 m is illustrated in Figure 12a. The solid and dashed lines represent the eigenvalue and the mean frequency value ( $\mu$ ) of the truck fleet, respectively. Additionally, the shaded area surrounding the dashed line indicates three times the standard deviation ( $\sigma$ ), i.e.,  $[\mu - 3\sigma, \mu + 3\sigma]$ , which means that 99.7% of the estimated forced frequencies are located within the highlighted area and frequency range [5.48, 5.56] Hz. Figure 12b makes the same comparison for the 5% crack at 7 m. As expected, the frequency range, [5.58, 5.66] Hz, is different for this second scenario, but the overall pattern remains.

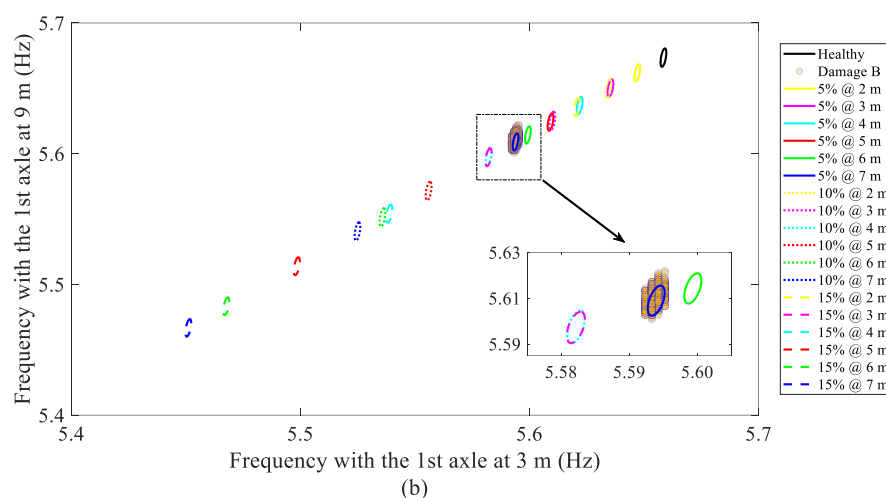




**Figure 12.** Comparison between transient forced-frequencies due to the crossing of 1000 trucks and eigenfrequencies for scenarios: (a) 15% crack at 5 m, and (b) 5% crack at 7 m.

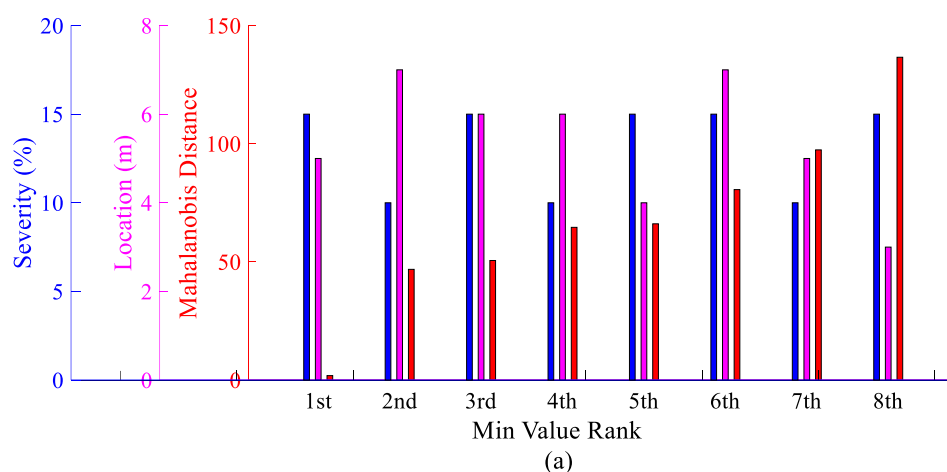
The points along the two vertical lines signaling the frequencies  $F_3$  and  $F_9$  in Figure 12 were selected for damage localization and quantification. Figure 13 plots the values of  $F_3$  and  $F_9$  obtained for the fleet of 3-axle trucks ( $p = 1000$ ) against the eigenfrequency database presented in Figure 6. Most of the points lie inside the ellipse from eigenvalue analysis corresponding to the true values of severity and location for both damage scenarios. For the smaller damage scenario, the ellipses associated with 5% crack at 6 m and 5% crack at 7 m are relatively close, but there is no difficulty in distinguishing the true solution. More challenging scenarios will display clusters of points falling within overlapping ellipses.

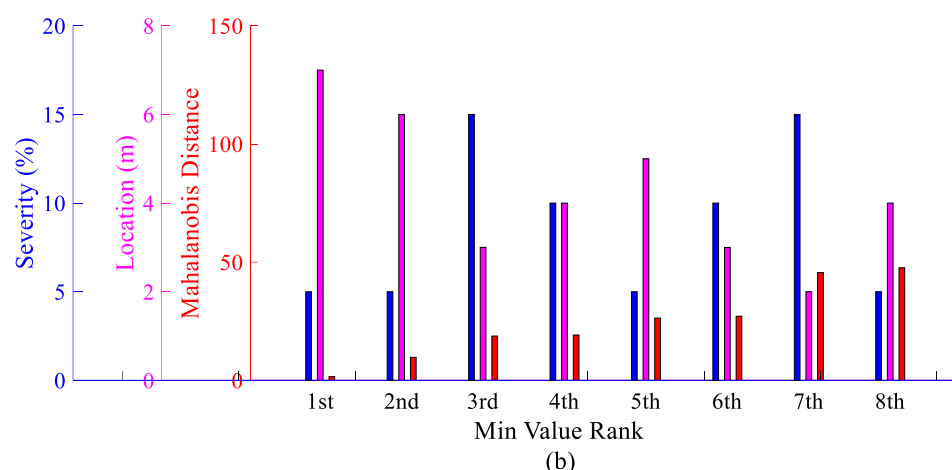




**Figure 13.** Comparison between transient forced-frequencies ( $F_3$ ,  $F_9$ ) due to the crossing of 1000 trucks and eigenvalue database for scenarios: (a) 15% crack at 5 m, and (b) 5% crack at 7 m.

The Mahalanobis distance provides a robust method to quantify the discordancy between frequencies in known-damage scenarios from eigenvalue analysis and unknown scenarios from transient analysis or measurements (steps (9) and (10) of the methodology). Figure 14 ranks the first 8 minimum values of the mean Mahalanobis distance for the two tested cracks when using  $p = 1000$  trucks. As expected, the first-ranked scenario matches the true damage severity and location in both scenarios. The size of the traffic fleet was varied,  $p = 1000, 500, 250, 100, 50, 25$  and 10 trucks, with no impact on accuracy. The insensitivity of the results to the size of the fleet is attributed to the separation between the distributions illustrated in Figure 13, and to the proximity of the measured frequencies to the ellipse holding the true solution.

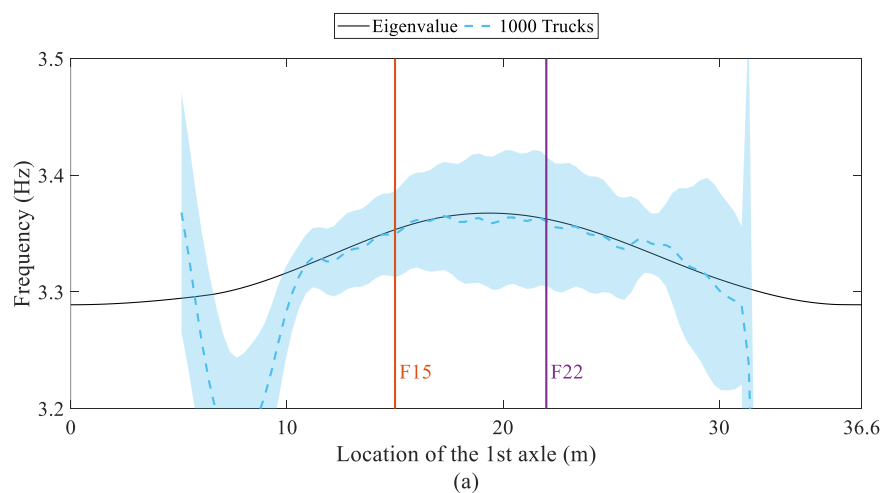




**Figure 14.** Min value rank of Mahalanobis distance for scenarios: (a) 15% crack at 5 m, and (b) 5% crack at 7 m.

### 6.2. Testing of a 30 m Bridge

The analysis from the previous section is extended here to a 30 m span bridge (2nd moment of area  $I = 2.2643 \text{ m}^4$  and mass per unit length  $m = 21,608 \text{ kg/m}$ ) traversed by a fleet of 3-axle trucks at a speed of 10 m/s. The first three longitudinal frequencies of the bridge in healthy condition are 3.385 Hz, 13.540 Hz, and 30.465 Hz. For comparison purposes, the damage scenarios have the same relative locations with respect to the total span as in Section 6.1, i.e., damage 'C' is a 15% crack located at 10 m, and damage 'D' is a 5% crack located at 14 m from the first support. Figure 15a,b compare the difference between the forced frequencies extracted from a fleet composed of  $p = 1000$  trucks and its associated eigenfrequencies for damages 'C' and 'D', respectively.



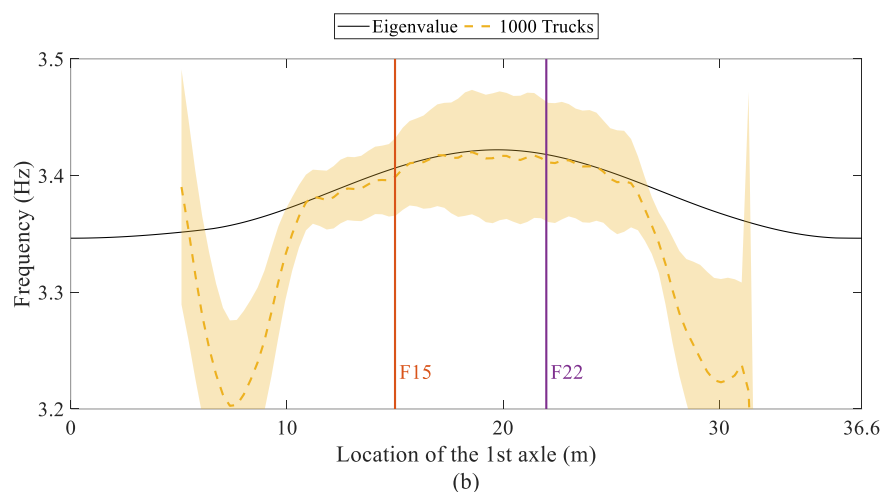


**Figure 15.** Comparison between transient forced-frequencies due to the crossing of 1000 trucks and eigenfrequencies for scenarios: (a) 15% crack at 10 m, and (b) 5% crack at 14 m.

As noted in the methodology section, the proper selection of the locations for frequency estimation is essential. It is clear from Figure 15 that the combination of frequencies used before, i.e.,  $F_3$  and  $F_9$ , does not work due to the edge effects caused by the axles entering and leaving the bridge. The higher speed has a negative impact on the estimation of the forced frequency by significantly widening the “blind spots” around the entrance and exit of vehicle axles. Nevertheless, there is a longer duration of available accelerations with respect to the 15 m bridge, making it possible to capture uncorrupted, instantaneous frequencies for positions of the front axle between 11 and 26 m. Therefore, the frequencies  $F_{15}$  and  $F_{22}$ , corresponding to positions of the front axle at 15 and 22 m from the start of the bridge, were proposed to establish the eigenfrequency database and the instantaneous frequencies from the dynamic transient analysis. As expected, the first bridge frequency decreased slightly more for damage ‘C’ than for damage ‘D’. For example, the range  $[\mu - 3\sigma, \mu + 3\sigma]$  within 11–26 m due to the 1000 trucks varies from 3.30 to 3.42 Hz for damage ‘C’, and from 3.35 to 3.47 Hz for damage ‘D’.

Figure 16a,b plot the 1000 values ‘measured’ for  $F_{15}$  and  $F_{22}$ , and their associated distributions for damages ‘C’ and ‘D’, respectively. Figure 16c,d show the ‘measurements’ for the two damages against the theoretical eigenfrequency database. In comparison to the 15 m bridge (Figure 13), there is considerable overlap between theoretical eigenvalue distributions associated with different damage scenarios. The reasons are twofold: (i) the change in the 1st bridge frequency due to damage is smaller in the 30 m bridge; and (ii) the standard deviations associated with  $F_{15}$  and  $F_{22}$  are larger than those associated with  $F_3$  and  $F_9$ . Regarding (i), even if equivalent damage scenarios cause a similar relative decrement in frequency for both spans, the absolute change in frequency is smaller in the longer span because of its lower first bridge frequency. For instance, damage ‘A’ in the 15 m bridge causes a reduction of  $-2.81\%$  in  $F_9$  with respect to a healthy condition, whereas damage ‘C’ in the 30 m bridge results in a similar change of  $-2.75\%$  in  $F_{22}$ . However, the former is equivalent to a drop of 0.16 Hz, while the latter only represents a reduction of 0.09 Hz. Regarding (ii), the standard deviations in the case of a healthy bridge are 0.0006 Hz, 0.0035 Hz, 0.0145 Hz, and 0.023 Hz, for  $F_3$  (15 m bridge),  $F_9$  (15 m bridge),  $F_{15}$  (30 m bridge), and  $F_{22}$  (30 m bridge), respectively. The locations of the frequencies selected in the 30 m bridge are closer to the middle of the duration of the signal, where the variability of the forced frequency due to the vehicle fleet is larger, i.e.,  $F_3$  and  $F_9$  exhibit a narrower shaded area in Figure 12 than  $F_{15}$  and  $F_{22}$  in Figure 15. Also, the variability for  $F_3$  is smaller than for  $F_9$ , which is closer to the middle of the signal. Indeed, the impact of the variability of the fleet on the first mode is felt more strongly when the vehicle is located

around the antinode, i.e., midspan. In any case, the majority of the fleet lies inside the ellipse from eigenvalue analysis corresponding to the true values of severity and location.

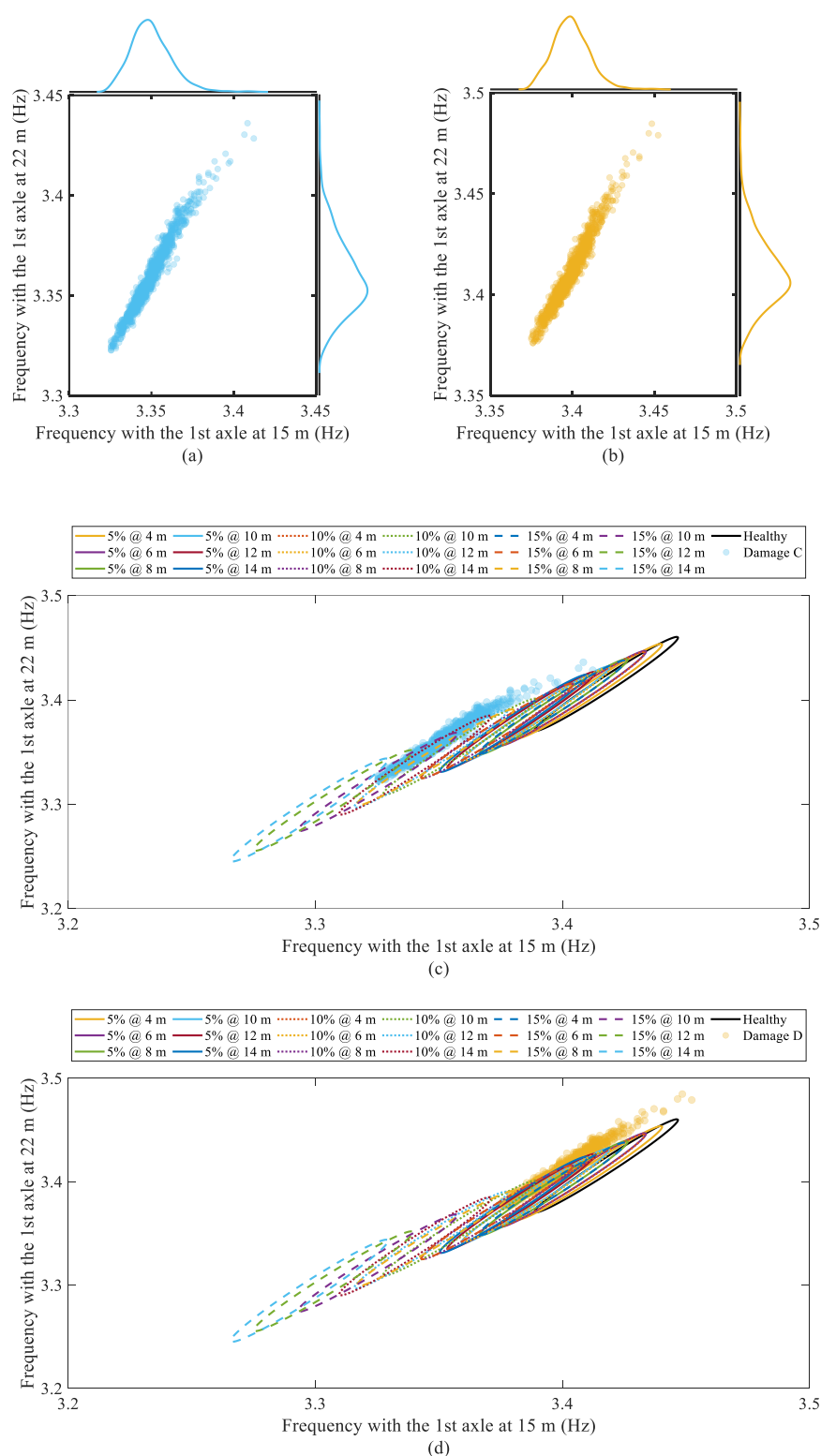


**Figure 16.** Comparison between transient forced frequencies ( $F_{15}$ ,  $F_{22}$ ) due to the crossing of 1000 trucks and eigenvalue database: (a) distributions of  $F_{15}$  and  $F_{22}$  for damage 'C', (b) distributions of  $F_{15}$  and  $F_{22}$  for damage 'D', (c) Damage 'C' against database, and (d) Damage 'D' against database.

Figure 17a,b rank the first 8 minimum values of the mean Mahalanobis distance with  $p = 1000$  trucks for damage scenarios 'C' and 'D', respectively. In contrast to the 15 m bridge (Figure 14), there are smaller differences between the Mahalanobis distances for the top ranked solutions due to a larger degree of variability in the 'measured' frequency due to the fleet, and a significant overlap between the statistical distributions of eigenfrequencies associated with each damage. The 1st ranked scenario matches the true damage severity and location in both scenarios, although differences between the 1st and 2nd ranked solutions are as small as 1.8290 vs. 1.9123 for damage 'C' (Figure 17a). In Figure 17b, the mean Mahalanobis distances for the first four ranked scenarios are 1.8363, 2.0133, 2.0306 and 2.0412.

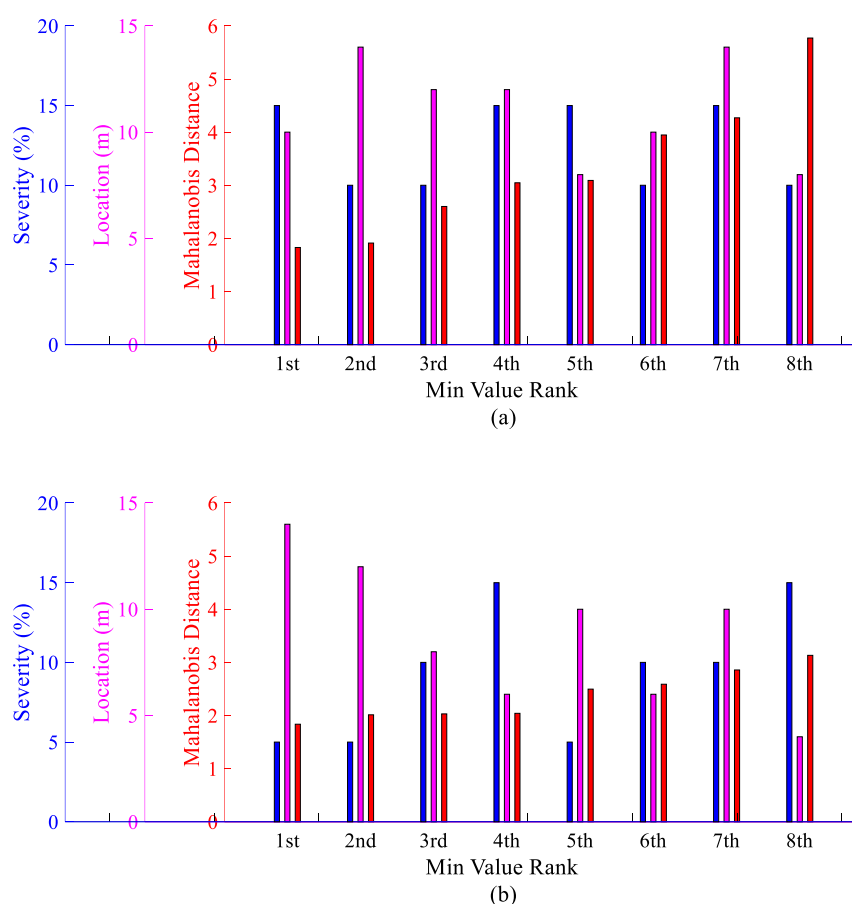


**Figure 17.** Min value rank of Mahalanobis distance for scenarios: (a) 15% crack at 10 m, and (b) 5% crack at 14 m.

Given that the Mahalanobis distances are relatively closer for the top ranked solutions, and are more difficult to distinguish in the 30 m bridge than in the 15 m bridge, the size of the traffic fleet was expected to have an impact that was not found for the 15 m bridge. Fleet sizes composed by  $p = 10, 25, 50, 100, 250, 500$  and 1000 trucks, were tested. Results indicate that the size does not have any impact on damage predictions for the damage scenario 'D'. Damage 'C' was accurately located and quantified for all fleet sizes, except for  $p = 25$  and  $p = 10$ , when it is characterized as a 10% crack located at 14 m, rather than a 15% crack at 10 m. A relatively high number of trucks is recommended to ensure a robust prediction of damage when the selected frequencies are sensitive to the variability of the fleet.



## 7. Conclusions

Level III damage detection methods can be achieved, in practice, using several dynamic parameters and a few modes of a bridge, yet their implementation is scarce due to the typically high number of sensors involved. The value of the frequency associated with the first mode of vibration of a bridge is easily extracted with only one or a few measurement sensors, but it is insufficient for locating and quantifying damage. Traditionally, a unique value of frequency is retained for a mode while taking a relatively long measurement period into account. However, this paper has demonstrated that the time-history of instantaneous forced frequencies associated with the different positions of a truck on a bridge stores information that makes damage identification possible.

Using eigenvalue analysis, a database of bivariate distributions of the first bridge eigenfrequencies associated with a truck fleet when the 1st axle of the vehicle is located at two different positions on the bridge was derived for different locations and severities of a crack. These distributions allow the visualization of how the frequencies of the bridge vary with crack location and crack severity, and they have accounted for some of the uncertainties related to the dynamic properties of a specific truck configuration. Instantaneous frequencies were calculated at the same two locations by applying a Hann-based STFT to the acceleration response of the bridge traversed by random trucks of the selected fleet. The instantaneous frequencies served to successfully locate and quantify two cracks when plotted over the wide range of bivariate distributions available from eigenvalue analysis. The Mahalanobis distance was proposed to discern scenarios where more than one solution was feasible.

The theoretical testing was limited to two damage scenarios (15% and 5% cracks located at 1/3 and 7/15 of the total span respectively), two speeds (1 m/s and 10 m/s) and two bridge spans (15 m and 30 m) with a smooth profile. Therefore, the 18 local damage scenarios included in the eigenvalue database covered the two crack scenarios tested in the two bridges. On the one hand, edge effects had a more profound impact in a shorter span, where the requirements for a lower speed are more strict in order to ensure a portion of uncorrupted frequencies sufficiently long. On the other hand, similar damages led to more uncertainty in the predictions for the longer span, where the size of the traffic fleet was proven to be a factor. It is acknowledged that there are multiple degradation processes that affect bridges other than cracks. In practice, there could be damage scenarios for which the eigenvalue database does not have associated distributions. As a result of the ideal testing conditions, only discrepancies between eigenvalue and transient analyses can move the measured frequencies away from the true distribution. It was shown that these discrepancies significantly increase for higher speeds and rougher profiles. Differences between theoretical models and reality, as well as noise in the measurements, also deteriorate the accuracy of the results. As a suggestion for further research, the methodology needs to be assessed with other damage scenarios, higher speeds, rough road profiles, modeling errors, and experimental data.

**Author Contributions:** Conceptualization, A.G., K.F. and M.C.; Formal analysis, A.G., K.F. and M.C.; Funding acquisition, A.G.; Investigation, A.G., K.F. and M.C.; Methodology, A.G., K.F. and M.C.; Project administration, A.G.; Resources, A.G.; Supervision, A.G.; Validation, K.F.; Visualization, A.G., K.F. and M.C.; Writing—original draft, K.F.; Writing—review & editing, A.G. and M.C. All authors have read and agreed to the published version of the manuscript.

**Funding:** This research was funded by Science Foundation Ireland, grant number 16/US/I3277.

**Institutional Review Board Statement:** Not applicable.

**Informed Consent Statement:** Not applicable.

**Data Availability Statement:** Some or all data, models, or code generated or used during the study are available from the corresponding author by request (MATLAB codes and data).

**Acknowledgments:** This research has received funding from Science Foundation Ireland (SFI)'s US-Ireland R&D partnership programme under the proposal id. 16/US/I3277 titled MARS-Fly.

**Conflicts of Interest:** The authors declare no conflict of interest.

## References

1. Doebling, S.W.; Farrar, C.R.; Prime, M.B. A summary review of vibration-based damage identification methods. *Shock. Vib. Dig.* **1998**, *30*, 91–105. <https://doi.org/10.1177/058310249803000201>.
2. Sinou, J.J. A review of damage detection and health monitoring of mechanical systems from changes in the measurement of linear and non-linear vibrations. In *Mechanical Vibrations: Measurement, Effects and Control*; Sapri, R.C., Ed.; Nova Science Publishers: Hauppauge, NY, USA, 2009; pp. 643–702.
3. Moughty, J.J.; Casas, J.R. A state of the art review of modal-based damage detection in bridges: Development, challenges, and solutions. *Appl. Sci.* **2017**, *7*, 510. <https://doi.org/10.3390/app7050510>.
4. Salawu, O.S. Detection of structural damage through changes in frequency: A review. *Eng. Struct.* **1997**, *19*, 718–723. [https://doi.org/10.1016/S0141-0296\(96\)00149-6](https://doi.org/10.1016/S0141-0296(96)00149-6).
5. Yang, Y.B.; Cheng, M.C.; Chang, K.C. Frequency variation in vehicle-bridge interaction systems. *Int. J. Struct. Stab. Dyn.* **2013**, *13*, 1350019. <https://doi.org/10.1142/S0219455413500193>.
6. Cantero, D.; Hester, D.; Brownjohn, J. Evolution of bridge frequencies and modes of vibration during truck passage. *Eng. Struct.* **2017**, *152*, 452–464. <https://doi.org/10.1016/j.engstruct.2017.09.039>.
7. Cantero, D.; McGettrick, P.; Kim, C.W.; O'Brien, E. Experimental monitoring of bridge frequency evolution during the passage of vehicles with different suspension properties. *Eng. Struct.* **2019**, *187*, 209–219. <https://doi.org/10.1016/j.engstruct.2019.02.065>.
8. Feng, K.; Gonzalez, A.; Casero, M. A kNN algorithm for locating and quantifying stiffness loss in a bridge from the forced vibration due to a truck crossing at low speed. *Mech. Syst. Signal Process.* **2021**, *154*, 107599. <https://doi.org/10.1016/j.ymssp.2020.107599>.
9. Cantero, D.; González, A. Bridge damage detection using weigh-in-motion technology. *J. Bridge Eng.* **2015**, *20*, 4014078. [https://doi.org/10.1061/\(ASCE\)Be.1943-5592.0000674](https://doi.org/10.1061/(ASCE)Be.1943-5592.0000674).
10. Sujon, M.; Dai, F. Application of weigh-in-motion technologies for pavement and bridge response monitoring: State-of-the-art review. *Automat. Constr.* **2021**, *130*, 103844. <https://doi.org/10.1016/j.autcon.2021.103844>.
11. Cebon, D. Design of multiple-sensor weigh-in-motion systems. *Proc. Inst. Mech. Eng. Part D-J. Automob. Eng.* **1990**, *204*, 133–144. [https://doi.org/10.1243/pime\\_proc\\_1990\\_204\\_145\\_02](https://doi.org/10.1243/pime_proc_1990_204_145_02).
12. Burnos, P.; Gajda, J.; Sroka, R.; Wasilewska, M.; Dolega, C. High accuracy Weigh-In-Motion systems for direct enforcement. *Sensors* **2021**, *21*, 8046. <https://doi.org/10.3390/s21238046>.
13. Yu, Y.; Cai, C.S.; Deng, L. State-of-the-art review on bridge weigh-in-motion technology. *Adv. Struct. Eng.* **2016**, *19*, 1514–1530. <https://doi.org/10.1177/1369433216655922>.
14. Rowley, C.W.; O'Brien, E.J.; González, A.; Žnidarič, A. Experimental testing of a moving force identification bridge weigh-in-motion algorithm. *Exp. Mech.* **2009**, *49*, 743–746. <https://doi.org/10.1007/s11340-008-9188-3>.
15. O'Brien, E.J.; Khan, M.A.; McCrum, D.P.; Žnidarič, A. Using statistical analysis of an acceleration-based bridge weigh-in-motion system for damage detection. *Appl. Sci.* **2020**, *10*, 663. <https://doi.org/10.3390/app10020663>.
16. Wang, S.; O'Brien, E.J.; McCrum, D.P. A novel acceleration-based moving force identification algorithm to detect global bridge damage. *Appl. Sci.* **2021**, *11*, 7271. <https://doi.org/10.3390/app11167271>.
17. O'Brien, E.J.; Brownjohn, J.M.W.; Hester, D.; Huseynov, F.; Casero, M. Identifying damage on a bridge using rotation-based Bridge Weigh-In-Motion. *J. Civ. Struct. Health Monit.* **2021**, *11*, 175–188. <https://doi.org/10.1007/s13349-020-00445-w>.
18. Shokravi, H.; Shokravi, H.; Bakhary, N.; Heidarrezaei, M.; Rahimian Koloor, S.S.; Petru, M. Vehicle-assisted techniques for health monitoring of bridges. *Sensors* **2020**, *20*, 3460. <https://doi.org/10.3390/s20123460>.
19. Ercolessi, S.; Fabbrocino, G.; Rainieri, C. Indirect measurements of bridge vibrations as an experimental tool supporting periodic inspections. *Infrastructures* **2021**, *6*, 39. <https://doi.org/10.3390/infrastructures6030039>.
20. Yang, M.; Liu, C. Possibility of bridge inspection through drive-by vehicles. *Appl. Sci.* **2021**, *11*, 69. <https://doi.org/10.3390/app11010069>.
21. Corbally, R.; Malekjafarian, A. Examining changes in bridge frequency due to damage using the contact-point response of a passing vehicle. *J. Struct. Int. Maint.* **2021**, *6*, 148–158. <https://doi.org/10.1080/24705314.2021.1906088>.
22. Corbally, R.; Malekjafarian, A. A data-driven approach for drive-by damage detection in bridges considering the influence of temperature change. *Eng. Struct.* **2022**, *253*, 113783. <https://doi.org/10.1016/j.engstruct.2021.113783>.
23. Matarazzo, T.J.; Santi, P.; Pakzad, S.N.; Carter, K.; Ratti, C.; Moaveni, B.; Osgood, C.; Jacob, N. Crowdsensing framework for monitoring bridge vibrations using moving smartphones. *Proc. IEEE* **2018**, *106*, 577–593. <https://doi.org/10.1109/Jproc.2018.2808759>.
24. Sitton, J.D.; Rajan, D.; Story, B.A. Bridge frequency estimation strategies using smartphones. *J. Civ. Struct. Health Monit.* **2020**, *10*, 513–526. <https://doi.org/10.1007/s13349-020-00399-z>.
25. Sarwar, M.Z.; Cantero, D. Deep autoencoder architecture for bridge damage assessment using responses from several vehicles. *Eng. Struct.* **2021**, *246*, 113064. <https://doi.org/10.1016/j.engstruct.2021.113064>.
26. Keenahan, J.; Ren, Y.F.; O'Brien, E.J. Determination of road profile using multiple passing vehicle measurements. *Struct. Infrastruct. Eng.* **2020**, *16*, 1262–1275. <https://doi.org/10.1080/15732479.2019.1703757>.
27. Khan, S.M.; Atamturktur, S.; Chowdhury, M.; Rahman, M. Integration of structural health monitoring and intelligent transportation systems for bridge condition assessment: Current status and future direction. *IEEE T. Intell. Transp.* **2016**, *17*, 2107–2122. <https://doi.org/10.1109/Tits.2016.2520499>.

28. González, A. Vehicle-bridge dynamic interaction using finite element modelling. In *Finite Element Analysis*; Moratal, D., Ed.; IntechOpen: London, UK, 2010; pp. 637–662. <https://doi.org/10.5772/10235>.
29. *Matlab R2022a*; The MathWorks, Inc.: Natick, MA, USA, 2022.
30. Roveri, N.; Carcaterra, A. Damage detection in structures under traveling loads by Hilbert–Huang transform. *Mech. Syst. Signal Process.* **2012**, *28*, 128–144. <https://doi.org/10.1016/j.ymssp.2011.06.018>.
31. Kim, H.; Melhem, H. Damage detection of structures by wavelet analysis. *Eng. Struct.* **2004**, *26*, 347–362. <https://doi.org/10.1016/j.engstruct.2003.10.008>.
32. Gul, M.; Catbas, F.N. Statistical pattern recognition for Structural Health Monitoring using time series modeling: Theory and experimental verifications. *Mech. Syst. Signal Process.* **2009**, *23*, 2192–2204. <https://doi.org/10.1016/j.ymssp.2009.02.013>.
33. Deraemaeker, A.; Worden, K. A comparison of linear approaches to filter out environmental effects in structural health monitoring. *Mech. Syst. Signal Process.* **2018**, *105*, 1–15. <https://doi.org/10.1016/j.ymssp.2017.11.045>.
34. Li, Y. *Factors Affecting the Dynamic Interaction of Bridges and Vehicle Loads*; University College Dublin: Dublin, Ireland, 2006.
35. O'Brien, E.J.; Keogh, D.L.; O'Connor, A. *Bridge Deck Analysis*, 2nd ed.; CRC Press: Boca Raton, FL, USA, 2015. <https://doi.org/10.1201/b17475>.
36. Barth, K.E.; Wu, H. Development of improved natural frequency equations for continuous span steel I-girder bridges. *Eng. Struct.* **2007**, *29*, 3432–3442. <https://doi.org/10.1016/j.engstruct.2007.08.025>.
37. Tilly, G.P. Dynamic behaviour of concrete structures Report of the RILEM 65-MDB Committee. *Mater. Struct.* **1986**, *19*, 460–460. <https://doi.org/10.1007/BF02472155>.
38. Castellanos-Toro, S.; Marmolejo, M.; Marulanda, J.; Cruz, A.; Thomson, P. Frequencies and damping ratios of bridges through Operational Modal Analysis using smartphones. *Constr. Build. Mater.* **2018**, *188*, 490–504. <https://doi.org/10.1016/j.conbuildmat.2018.08.089>.
39. Sinha, J.K.; Friswell, M.I.; Edwards, S. Simplified models for the location of cracks in beam structures using measured vibration data. *J. Sound Vib.* **2002**, *251*, 13–38. <https://doi.org/10.1006/jsvi.2001.3978>.
40. Christides, S.; Barr, A.D.S. One-Dimensional Theory of Cracked Bernoulli-Euler Beams. *Int. J. Mech. Sci.* **1984**, *26*, 639–648. [https://doi.org/10.1016/0020-7403\(84\)90017-1](https://doi.org/10.1016/0020-7403(84)90017-1).
41. Maeck, J.; Wahab, M.A.; Peeters, B.; De Roeck, G.; De Visscher, J.; De Wilde, W.P.; Ndambi, J.M.; Vantomme, J. Damage identification in reinforced concrete structures by dynamic stiffness determination. *Eng. Struct.* **2000**, *22*, 1339–1349. [https://doi.org/10.1016/S0141-0296\(99\)00074-7](https://doi.org/10.1016/S0141-0296(99)00074-7).
42. Law, S.S.; Zhu, X.Q. Dynamic behavior of damaged concrete bridge structures under moving vehicular loads. *Eng. Struct.* **2004**, *26*, 1279–1293. <https://doi.org/10.1016/j.engstruct.2004.04.007>.
43. Kim, C.W.; Kawatani, M.; Kim, K.B. Three-dimensional dynamic analysis for bridge-vehicle interaction with roadway roughness. *Comput. Struct.* **2005**, *83*, 1627–1645. <https://doi.org/10.1016/j.compstruc.2004.12.004>.
44. Grave, S. *Modelling of Site-Specific Traffic Loading on Short to Medium Span Bridges*; Trinity College Dublin: Dublin, Ireland, 2001.
45. Cantero, D.; González, A.; O'Brien, E.J. Comparison of bridge dynamic amplifications due to articulated 5-axle trucks and large cranes. *Balt. J. Road. Bridge. Eng.* **2011**, *6*, 39–47. <https://doi.org/10.3846/bjrbe.2011.06>.
46. Scania. Available online: <https://www.scania.com/content/dam/scanianoe/market/uk/brochures/truck/spec-sheets/p-series/spec-sheet-scania-p250db6x2mna.PDF> (accessed on 30 September 2022).
47. RSA. Available online: <https://www.rsa.ie/road-safety/road-users/professional-drivers/vehicle-safety-legislation/weights-and-dimensions> (accessed on 30 September 2022).
48. Cebon, D. *Handbook of Vehicle-Road Interaction*; CRC Press: Boca Raton, FL, USA, 1999; p. 616.
49. White, W. *Natural Frequency of Pickups and Medium and Heavy Trucks for Use in Component Design*; Advanced Highway Maintenance and Construction Technology (AHMCT) Research Center, University of California: Davis, CA, USA, 2018.
50. Peeters, B.; De Roeck, G. One-year monitoring of the Z24-Bridge: Environmental effects versus damage events. *Earthq. Eng. Struct. Dyn.* **2001**, *30*, 149–171. [https://doi.org/10.1002/1096-9845\(200102\)30:2<149::AID-EQE1>3.0.CO;2-Z](https://doi.org/10.1002/1096-9845(200102)30:2<149::AID-EQE1>3.0.CO;2-Z).
51. Gunawan, T.S. On the optimal window shape for genomic signal processing. In Proceedings of the 2008 International Conference on Computer and Communication Engineering, Kuala Lumpur, Malaysia, 13–15 May 2008; pp. 252–255. <https://doi.org/10.1109/ICCCE.2008.4580606>.
52. Amezcua-Sanchez, J.P.; Adeli, H. Signal processing techniques for vibration-based health monitoring of smart structures. *Arch. Comput. Method Eng.* **2016**, *23*, 1–15. <https://doi.org/10.1007/s11831-014-9135-7>.
53. González, A.; O'Brien, E.J.; McGetrick, P.J. Identification of damping in a bridge using a moving instrumented vehicle. *J. Sound Vib.* **2012**, *331*, 4115–4131. <https://doi.org/10.1016/j.jsv.2012.04.019>.
54. Frýba, L. *Vibration of Solids and Structures under Moving Loads*, 3rd ed.; Thomas Telford: London, UK, 1999.
55. Yang, Y.B.; Wang, B.; Wang, Z.; Shi, K.; Xu, H. Scanning of bridge surface roughness from two-axle vehicle response by EKF-UI and contact residual: Theoretical study. *Sensors* **2022**, *22*, 3410. <https://doi.org/10.3390/s22093410>.
56. ISO 8608:2016; Mechanical Vibration—Road Surface Profiles—Reporting of Measured Data. ISO: Geneva, Switzerland, 2016; p. 36.